Enabling Long Range Underwater Backscatter via Van Atta Acoustic Networks

Aline Eid[*†§], Jack Rademacher[*†], Waleed Akbar[†], Purui Wang[†], Ahmed Allam[†], and Fadel Adib[†]

[†]Massachusetts Institute of Technology, [§]University of Michigan

[*]Co-primary Authors

{alineeid,jradema,wakbar,prwang,allam,fadel}@mit.edu

ABSTRACT

We present the design, implementation, and evaluation of Van Atta Acoustic Backscatter (VAB), a technology that enables long-range, ultra-low-power networking in underwater environments. At the core of VAB is a novel, scalable underwater backscatter architecture that bridges recent advances in RF backscatter (Van Atta architectures) with ultra-low-power underwater acoustic networks. Our design introduces multiple innovations across the networking stack, which enable it to overcome unique challenges that arise from the electro-mechanical properties of underwater backscatter and the challenging nature of low-power underwater acoustic channels. We implemented our design in an end-to-end system, and evaluated it in over 1,500 real-world experimental trials in a river and the ocean. Our evaluation in stationary setups demonstrates that VAB achieves a communication range that exceeds 300m in round trip backscatter across orientations (at BER of 10^{-3}). We compared our design head-to-head with past state-of-the-art systems, demonstrating a 15× improvement in communication range at the same throughput and power. By realizing hundreds of meters of range in underwater backscatter, this paper presents the first practical system capable of coastal monitoring applications. Finally, our evaluation represents the first experimental validation of underwater backscatter in the ocean.

CCS CONCEPTS

• **Networks** → Network architectures; • **Hardware** → **Wireless integrated network sensors**; *Beamforming*; • **Applied computing** → *Earth and atmospheric sciences*;

KEYWORDS

Van Atta, Retrodirective Structures, Backscatter Communications, Piezo-Acoustic Backscatter, Ocean IoT, Underwater Sensing.

(a) Past Underwater Backscatter   **(b) Our Retro-reflective Design**

Figure 1: Underwater backscatter designs. (a) Existing designs are inefficient since a node backscatters in all directions. (b) Our efficient design reflects the impinging signal back to the projector-hydrophone pair.

1 INTRODUCTION

Over the past few years, there has been growing interest in low-power, long-range underwater networks [1–5]. Such networks can open up various applications spanning underwater climate change monitoring, global food production, coastal monitoring, marine life discovery, and extraterrestrial exploration [6–10]. For example, a submerged network of underwater sensors can continuously measure ocean vital signs (temperature, pressure, and dissolved carbon dioxide) to create more accurate climate change models [11, 12] and monitor the efficacy of carbon capture technologies [13, 14]. Underwater sensor networks can be particularly helpful in coastal deployments where spatiotemporal measurements of temperature and pressure would improve hurricane predictions and support disaster response [15]. Near-coast underwater sensor deployments can also be used to monitor acidity and temperature in aquaculture farms (e.g., fish farms) to support early detection of environmental hazards such as harmful algae blooms [16]. These broad-reaching implications for underwater sensing technologies have resulted in major funding initiatives for ocean IoT by DARPA [17], NSF [18], and venture capital firms, which announced new funds totaling over $200 million in the last year alone [19, 20].

One of the most promising technologies that has emerged to realize this vision of a low-cost, energy-autonomous ocean IoT is underwater backscatter [1–4]. Underwater backscatter nodes differ from traditional underwater communication technologies in that they communicate by *reflecting* rather than *generating* acoustic signals; such a communication mechanism makes them about a million times more energy-efficient than prior state-of-the-art low-power underwater acoustic modems, even at the same data rates [3]. However, a key challenge that still faces scaling underwater backscatter to practical deployment is their limited communication range. In particular, state-of-the-art implementations have only demonstrated few to tens of meters of range, which makes it

difficult to deploy these technologies at scale, even in near-shore settings such as those used in coastal monitoring, disaster response, or aquaculture farms, which typically require deployments at a few hundred meters offshore [21].

This paper introduces Van Atta acoustic backscatter (VAB), a new networking architecture for underwater backscatter that enables ultra-low-power, long-range underwater networking. Our architecture inherits the benefits of underwater backscatter, and operates similar to prior designs by modulating acoustic reflections. Its key innovation lies in how it modulates these reflections - through a *retroreflective* structure - which allows it to boost the communication range of underwater backscatter by up to an order of magnitude over state-of-the-art designs.

Before introducing our new design, it is helpful to understand why it is difficult for underwater backscatter systems to communicate over a long range. Consider the illustrative example in Fig. 1a. Here, a projector transmits an acoustic signal; when the signal reaches a backscatter node, the node reflects it in all directions, and a portion of this reflection arrives at the hydrophone receiver. To communicate, the backscatter node modulates its reflection coefficient, which allows the receiving hydrophone to sense changes in reflections and use them to decode the node's messages.

A key factor that limits the range of underwater backscatter communication is the spherical spreading of the backscattered signal traveling from the node back to the hydrophone. Specifically, when an underwater node backscatters the downlink signal, this backscatter does not only go back to the hydrophone receiver but rather scatters - or spreads - in all directions, as can be seen in Fig. 1a. Because the backscattered signal spreads in all directions, the amount of power that arrives back to the hydrophone ends up being a very small fraction of the one that originally arrived at the backscatter node. This power loss significantly degrades the signal-to-noise ratio (SNR) of the received signal and is the key factor that limits the range of underwater backscatter systems.

A classical approach to overcome such power loss (due to spherical spreading) is to perform active beamforming, whereby communication signals are focused in the direction of the link between a transmitter and receiver. Indeed, beamforming is commonly used in underwater point-to-point communication (and SONAR) systems and is typically implemented using phased arrays. However, such beamforming is too power-hungry and complex for backscatter nodes. This is because it requires active control of the different phase elements; it also typically requires searching for the direction of alignment between the transmitter and receiver. Thus, while one could in principle apply such beamforming at the projector and hydrophone, performing it at the backscatter node itself would be power-hungry and computationally expensive, making it undesirable for these passive nodes.

To address this challenge, we developed a new class of underwater backscatter systems that are passive and retrodirective. Specifically, rather than scattering the incoming signal in all directions, our nodes passively reflect an impinging acoustic signal back toward the source. Fig. 1b illustrates this idea. In this figure, a signal that arrives at a direction θ, is retrodirected back toward a hydrophone in that same direction. Such an approach would mitigate the spherical loss on the uplink, making the overall design much more efficient, and allowing for longer-range communications.

(a) RF Van Atta **(b) Piezo Van Atta**
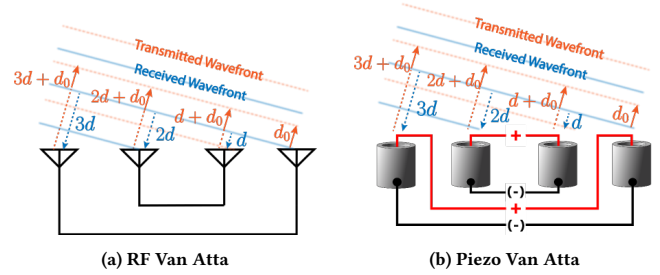
Figure 2: Van Atta Structures. (a) By connecting antennas symmetrically, the received signal is re-transmitted in the same direction. (b) We realize the same concept via differential connections with piezo-acoustic nodes.

To bring the concept of retrodirectivity to underwater backscatter, we exploit a concept called Van Atta arrays. Van Atta arrays were introduced in the 1950's for passive RF (Radio frequency) retrodirectivity [22] and have recently been also applied for millimeter waves in the networking community [23, 24]. In Van Atta structures, every symmetric pair of antenna elements are connected to each other, as shown in Fig. 2a. Because of this symmetric structure, a signal arriving at the array is retrodirected back to the source, effectively creating the same effect as active beamforming, albeit using an entirely passive structure. Intuitively, this is because the total path traversed by the wavefront is the same across all antenna pairs (in Fig. 2a, it is $d_0 + 3d$).

However, bringing Van Atta structures to underwater backscatter is challenging, primarily due to the electromechanical properties of underwater backscatter nodes. First, these nodes are fabricated from piezoelectric materials, whose performance is highly reliant on the coupling between their electrical and mechanical components. Thus, unlike a pair of RF antennas which can be easily connected to each other to allow a signal to pass through them for retrodirectivity, directly connecting a pair of piezoelectrics to each other (as shown in Fig. 2b) would shift their resonance and drastically degrade their performance. Second, in order to operate at a desired resonant frequency (e.g., 20 kHz acoustics), these nodes need to have certain volumetric structures, similar to the cylinders shown in Fig. 2b. As a result, placing multiple resonant nodes in close proximity causes them to block each other's acoustic signals and causes the underwater sound to diffract around their volumetric structures, creating new interactions that degrade the beamforming gain in ways that antenna Van Attas do not experience. These challenges are exacerbated by the difficulty of fabricating piezoelectric nodes to be electrically matched and the node's differential nature. Given all this, it is difficult to design even a single-pair of underwater acoustic Van Atta retroreflective structures, let alone to scale these structures into multi-node array.

To overcome the above challenges, our design introduces innovations at both the unit-cell level (i.e., a pair of piezoelectrics) and the overall node architecture:

- At the unit-cell level, we introduce a new Van Atta backscatter structure that carefully orchestrates how the signal passes between any two connected piezoelectric nodes in order to maintain their individual high-performance properties while enabling retrodirective backscatter. This is realized by introducing 2 key innovations: the first is a transformer-based matching network that

allows maximal power transfer between the nodes while maintaining their optimal electromechanical properties for resonance; the second is a cross-polarity differential switching mechanism where modulation is performed by alternating the polarities of the piezoelectric materials (rather than simply opening/closing a single switch as in RF Van Atta). We describe this structure in detail in §3.1, and how it enables maximizing the SNR of the backscattered response in §3.2, thus boosting the uplink range (and throughput).

- At the node architecture level, we develop a design that can scale the gain of retrodirectivity with the number of piezoelectric transducers (N). Building on our above basic-unit design consisting of two transducers, we extended our retrodirective structure to an array of units that allows achieving a higher retrodirectivity gain. Here, we solve the problem of occlusion by implementing the concept of staggering (described in §3.3). We then extend our 1D array to a 2D array with an orientation-agnostic behavior, enabling 3D retrodirectivity (described in §3.4).

We implemented a prototype of VAB and tested it in different environments spanning a river and the Atlantic ocean. We mechanically fabricated our transducers in-house and designed a custom circuit board to perform the switching and the matching. We implemented a robust decoding pipeline consisting of a multichannel adaptive decision feedback equalizer [25] to combat inter-symbol interference (ISI). The end-to-end system consists of a projector and a multichannel receiver array with 7 hydrophones, in addition to the Van Atta backscatter nodes. We implemented and evaluated different sizes and geometries of underwater Van Atta structures (including 2-element, 4-element, and 8-element arrays) to understand their performance across the design space. Our evaluation was performed in stationary setups across a wide range of rotations, distances, communication throughputs, and projector power levels. Our evaluation across over 1,500 real-world experimental trials demonstrates the following:

- VAB achieves a communication range of 300 m round-trip at BER of 10^{-3} at throughputs of 500 bps (which are standard throughputs for underwater acoustic communication [26]). In contrast, at the same throughput and power level, a state-of-the-art underwater backscatter system is limited to 20 m round-trip range at BERs of 10^{-2}. This shows that VAB boosts the range of underwater backscatter by more than 15× over prior state-of-the-art designs.

- VAB is capable of 3D retrodirectivity. Specifically, when evaluated across different orientations, it achieves a median BER of 8.8×10^{-4}; this is 30× better than a standard array-based implementation, which achieves a median BER of 2.6×10^{-2} at the same range and throughput.

- Our design of VAB is scalable, as evidenced in our empirical evaluation of arrays of different sizes and shapes, and its gain increases with the number of array elements.

Contributions: VAB is the first retrodirective underwater backscatter technology. Its design introduces multiple innovations – including cross-polarity switching, transformer-based matching, and staggering – to the field of underwater backscatter, which enables it to bring the concept of Van Atta structures to low-power underwater communications. The paper also contributes the implementation

and evaluation of multiple VAB prototypes, and an end-to-end system including an underwater backscatter reader with a multi-channel decoder. Finally, the paper presents the first practical realization of underwater backscatter at a few hundred meters and the first empirical validation of backscatter in the ocean.

It is worth noting that the results reported in this paper do not demonstrate the full potential of our VAB system. Specifically, our evaluation was limited by the width of our docks (in the river and the ocean), and future work would need to test the design further into the ocean. Nonetheless, the paper marks a new milestone in enabling ultra-low-power, long-range underwater networking systems.

2 BACKGROUND & RELATED WORK
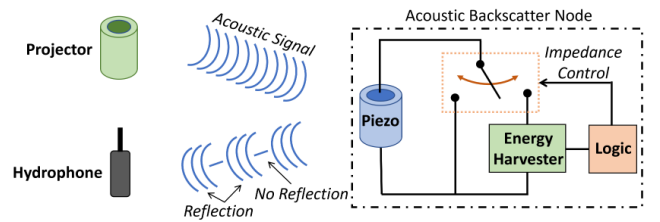
Figure 3: Piezo-Acoustic Backscatter. A node communicates bits of zero and one by switching the impedance control. It can harvest energy when the switch is connected to the energy harvester.

(a) Underwater Backscatter: Underwater backscatter is a recently-introduced communication technology that enables ultra-low-power underwater communication. The basic operation of underwater backscatter is shown in Fig. 3. Each node has a piezoelectric material which can be switched between two states (reflective and non-reflective) to communicate data in binary; such switching can be done using a transistor. When a projector transmits sound on the downlink, its reflection is modulated using the backscatter switching and received and decoded using an underwater hydrophone.

Electrically, the backscatter node changes the reflection coefficient of the piezoelectric material by switching the load impedance Z_L between closed (zero) and a matched load ($Z_L = Z_S^*$, where Z_S^* is the conjugate of the piezoelectric source impedance Z_S). Specifically, the reflected power P_r can be expressed through the following equation [3]:

$$P_r = \left| \frac{Z_L - Z_S^*}{Z_L + Z_S} \right|^2 P_i \tag{1}$$

where P_i is the incident power.

Prior work has shown that underwater backscatter enables building battery-free underwater sensor nodes. By incorporating an energy harvesting unit (as in Fig. 3), these nodes can harvest energy in their absorptive state and use it to power up ultra-low-power embedded designs. Further work has shown how one could improve the bandwidth of underwater backscatter [21], achieve higher-order modulation [27], perform localization via underwater backscatter [28], and perform wireless underwater imaging using this technology [29]. Despite these advances, the communication range of underwater backscatter remains limited to within few to tens of meters, and there is still a need to develop solutions that enable

longer-range communication to drive these technologies to their full potential.

(b) Acoustic Arrays: Acoustic arrays are commonly used in underwater communication and SONAR systems [30]. These systems can focus their energy in a specific direction (i.e., beamform), which enables them to achieve higher ranges than single-element omnidirectional acoustic transducers. Such beamforming can be achieved using phased array architectures, where the phases for each individual element are actively controlled to steer the beam in a desired direction. While implementing active beamforming on the projector and hydrophone is practical, applying the same techniques on the passive backscatter nodes would significantly increase their power consumption and complexity. This work brings the benefits of beamforming to backscatter nodes to extend their communication range, but without increasing their power consumption and computational complexity.

(c) RF Retrodirectivity: Retrodirectivity (used interchangeably in this work with *retroreflectivity*) refers to the concept of reflecting an impinging signal back to the source that it came from [31]. In recent years, researchers in the networking community have leveraged structures like Van Atta and Rotman lens to develop retrodirective RFID tags that can achieve long range communications at RF and millimeter-wave frequencies [24, 32, 33]. The RF Van Atta structure consists of an array of antennas interconnected in symmetrical pairs. It is worth noting that past work has considered building underwater acoustic mirrors [34, 35]; however, none of these could be used to communicate or backscatter data. Thus, this work is the first to bring retrodirective backscatter communication to acoustic arrays, and it does so in the context of underwater backscatter.

3 DESIGN

This section first describes the design and implementation of the core Van Atta structure (unit cell), then describes how to extend it to arrays and 3D retrodirectivity.[1]

3.1 Van Atta Unit Cell

To understand the challenges in bringing the Van Atta to underwater backscatter, let us first understand the basic RF Van Atta unit cell, shown in Fig. 4 with two standard (50 Ω) antennas. In this design, two switches are used to either connect the two antennas to each other (to retroreflect an incoming signal) or to 50 Ω loads (to absorb the incoming signal). This switching technique is known as pass/absorb. The switches are simultaneously controlled to alternate between these 2 states to achieve retroreflective backscatter.

However, applying the same idea in underwater backscatter is not that simple. First, unlike antennas, which typically have one main external feeding point (i.e., are single-ended), piezoelectric transducers are differential. Therefore, we need a new switch architecture to alternate between different reflective/absorptive states and optimize the backscatter signal-to-noise ratio (SNR). Second, aside from the need for a novel switching architecture, the piezoelectric transducers need to be matched to maximize the retroreflective SNR. Unlike antennas which can be easily designed or purchased to have 50 Ω or 75 Ω impedance, it is very difficult to design a piezoelectric transducer to have an impedance that is (1) real and

---

[1]This work does not raise any ethical issues.
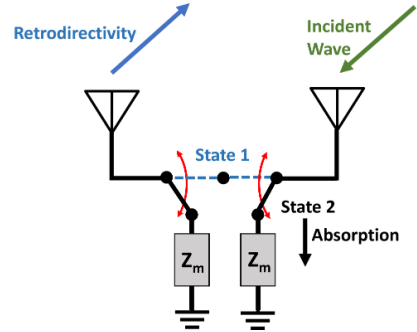
Figure 4: Antenna-based modulated Van Atta. The unit cell Van Atta consists of two antennas, matched loads (Z_m), and switches to modulate the reflection coefficient based on the pass/absorb switching technique.

(2) consistent. This is because (1) a piezoelectric device is capacitive by nature, and (2) even with tight mechanical tolerances, the fabrication of a sealed transducer results in significant process variations in the measured impedance. Therefore, it is unrealistic to expect maximum power transfer between the direct connection of two acoustic nodes.

In the following, we describe two ways of switching the piezo-acoustic nodes and their impact on the retrodirectivity performance. Intuitively, the performance of the backscatter system is better when the difference between the two states (e.g., "reflective" and "non-reflective") is highest. This is because a larger difference between the states allows a hydrophone to more easily distinguish between them. This can be formalized using a metric called the modulation factor M and expressed using the following equation:

$$M \quad |\Gamma_{state1} \quad \Gamma_{state2}|^2 \tag{2}$$

where Γ_{state1} and Γ_{state2} are the reflection coefficients, assessed at the hydrophone, of the modulation states.

For simplicity, in what follows, we first focus on the switching architecture (while ignoring the matching) then we describe how to extend it with a matching network between the nodes of the unit cell.

Option 1: Pass/Reflect Switching. Let us first explore the simplest form of switching and see why it wouldn't work for retrodirective backscatter. The simplest form of switching is to turn the switch "ON" and "OFF", also known as pass/reflect, shown in Fig. 5. Consider the reflection coefficient in each of these states:

- In the "OFF" state (shown as state 1) when the switch is open, the incoming wave faces an open load, and the wave is fully reflected back via each node back to the hydrophone. As a result, Γ_{state1} 1.
- In the "ON" state (shown as state 2), the node's terminals are connected to form a Van Atta pair. Here, the received signal by one node is transmitted through the wire and then emitted by the second node back to the hydrophone.[2] Therefore, in this state, a wave received by one node is re-emitted by the other, resulting in a full reflection from the adjacent node and an effective reflection

---

[2]Because the frequency is very low (a few kHz), the phase offset that the signal undergoes through the wire is negligible. For example, at f=20 kHz and d=1m length wire yields a phase change of $2\pi d/\lambda$=0.0004 radians, where λ c/f and c is the speed of RF in the wire, i.e., 3×10^8 m/s.
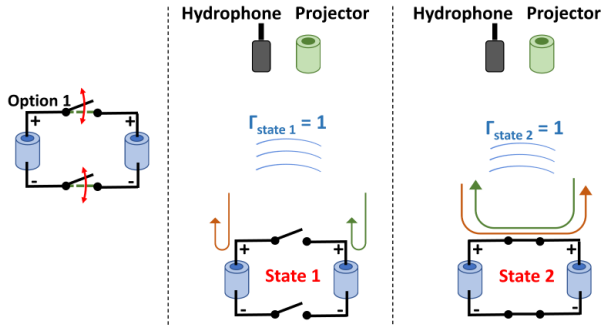
Figure 5: Option 1: Pass/Reflect Switching. When switches are open, the hydrophone sees a reflection coefficient Γ_{state1} of 1. When switches are closed, the hydrophone also sees a reflection coefficient Γ_{state2} of 1. Since $\Gamma_{state1} = \Gamma_{state2} = 0$, the hydrophone can't detect the backscattered response.

Figure 6: Option 2: Cross-Polarity Switching. When switches connect like-polarities, the hydrophone sees a $\Gamma_{state1} = 1$. When switches connect cross-polarities, the hydrophone sees a $\Gamma_{state2} = -1$.This yields the highest modulation factor of 4, resulting in a highly detectable backscattered response.

seen at the hydrophone of $\Gamma_{state2} = 1$.

While this switching approach offers a Van Atta behavior in the "ON" state, the reflections coming from states 1 and 2 may be identical in amplitude and phase at the hydrophone at multiple angles, with $\Gamma_{state1} = 1$, and $\Gamma_{state2} = 1$. This yields a modulation factor value of 0 (per Eq. 2), and results in no detectability and (very low) SNR at the hydrophone.[3] Hence, we need a different switching mechanism.

Option 2: Cross-Polarity Switching. In the second switching technique, we implemented a mechanism that maintains the connection between the two nodes "ON" at all times, but toggles it between in-phase and counter-phase polarities. This idea is shown in Fig. 6. Notice that each of two transducers have a positive (+) and negative (-) terminal. Let us look at the reflection coefficient in each of these states:
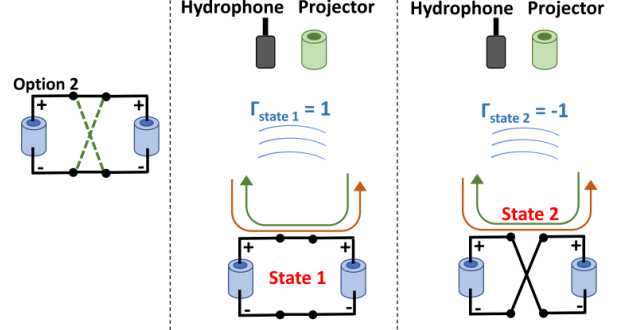
- In state 1, the nodes' terminals are connected to form a Van Atta pair with like-polarity (positive-to-positive and negative-to-negative), similar to state 2 described in the previous switching mechanism. Therefore, the effective reflection expected at the hydrophone is $\Gamma_{state1} = 1$.
- In state 2, the Van Atta pairs are connected in cross-polarity (i.e., positive-to-negative and negative-to-positive). Here, due to cross-polarity, the phase of the reflected wave emitted from the Van Atta is 180° shifted from the one created due to state 1 (since reversing the voltage polarities creates an out-of-phase wave). In other words, the effective reflection coefficient at the receiver is $\Gamma_{state2} = -1$.

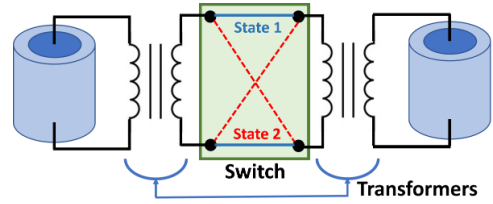In this switching architecture, the modulation factor is:

$$M = |\Gamma_{state1} - \Gamma_{state2}|^2 = |1 - (-1)|^2 = 4 \quad (3)$$

This means that this switching architecture results in the highest possible modulation factor (since the maximum magnitude of the reflection coefficient is 1). Thus, this architecture has the highest detectability and highest SNR at the hydrophone, and we use it to design our switching network. Appendix B empirically compares different switching mechanisms, demonstrating the superiority of

Figure 7: Van Atta Unit Cell. A unit cell consists of two piezos, two transformers, and a cross-polarity switch.

our cross-polarity approach irrespective of the angle of incidence.

Transformer-Based Matching Network. So far, our discussion of switching networks ignored the impact of the piezoelectric transducer's impedance. In practice, this impedance is highly capacitive and has significant variability across transducer design (unlike RF, where elements can be easily matched to 50 Ω). Thus, we need a mechanism to ensure matching for proper Van Atta operation.

To see why impedance matching is critical, recall that the operation of the Van Atta depends on the ability of the signal to pass through from one node to another (as seen in Figs.4 and 6). Formally, we need the electrical power of one node to be entirely transferred to the other node, and vice-versa. The power delivered from one node to the other is given by:

$$P_L = V_0^2 \frac{R_L}{2|Z_L + Z_S|^2} \quad (4)$$

where Z_L is the impedance of the node receiving power, $R_L = \text{Re}\{Z_L\}$, Z_S is the impedance of the node delivering power. To maximize P_L, we need to minimize $|Z_L + Z_S|^2$. This is achieved by setting $Z_L = Z_S^*$.[4]

To address these problems, we integrated a transformer-based matching network between each node in every pair as shown in Fig. 7. We set the magnetizing inductance of each transformer using the following equation:

$$L_m = \frac{|Z_N|^2}{\text{Im}\{Z_N\}\omega} \quad (5)$$

where Z_N is the node impedance and ω is the angular frequency.

---

[3]Note that this does not mean that the SNR would be very low at *all* angles, but that there exists many angles where the retrodirectivty gain would be negative (as we demonstrate empirically in Appendix B).

[4]See Appendix C for a detailed analysis on the impact of impedance mismatch on the beams generated by the retrodirective structure.
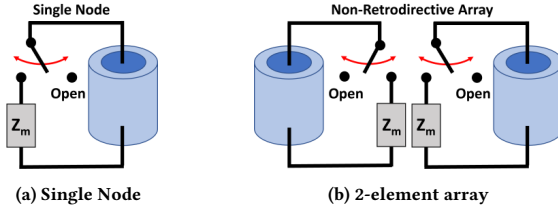
Figure 8: Baseline Designs. (a) Single node switching between open and matched load states. (b) 2-element array (both simultaneously) switched between open and matched load states.

Figure 9: SNR vs Angle. The channel SNR (dB) plotted vs. azimuth angle of a single node (red), array (yellow), and Van Atta (blue).

With this method, we create an end-to-end match transforming the highly capacitive, complex-valued node impedance into one that is entirely real.[5]

This solution optimizes the uplink SNR and eliminates the need for large inductors (which are difficult to source) and enables full DC isolation between the node and the switching circuitry, since power transfer in a transformer is achieved through magnetic coupling.

3.2 Validating Our Unit Cell

To validate our design, we implemented a basic Van Atta unit cell (of Fig. 7) consisting of two piezoelectric transducers that we fabricated in-house, a breadboard involving the design of the Van Atta switching mechanism using the TS5A23160 analog switch [36], and the transformer-based matching. The chip is a dual single-pole double-throw (SPDT) switch, configured to achieve cross-polarity switching. We chose a frequency of 18.5 kHz, close to the resonance frequency of the piezoelectric cylinder in our transducer, to optimize the radiation efficiency and performance of the node. Based on the frequency choice, we measured the impedance of the node in the river–our testing environment–to design our transformer-based matching network.

We compared three designs:

- *Single-node Fig. 8a)*: The first was a simple single transducer backscatter node. The single element was switched between the following two states: open load and a matched load Z_M, in a manner similar to past work [3, 21].
- *2-element array Fig. 8b)*: The second was a simple 2-element array, consisting of 2 elements next to each other and separated by λ.[6] The two switches were controlled simultaneously. Specifically, we applied the same Open/Matched switching performed on the single node, but instead on two nodes simultaneously.
- *Van Atta unit cell Fig. 7)*: The third is our Van Atta unit cell of 2 elements with cross-polarity.

We evaluated whether the Van Atta unit cell has the potential to satisfy these two desired properties: improved SNR over a single element, and retrodirectivity vs incidence angles compared to the basic 2-element array. Thus, we performed an experiment in a river to compare the above three designs. In this experiment, we used a piezoelectric transducer fabricated in-house as a projector, an
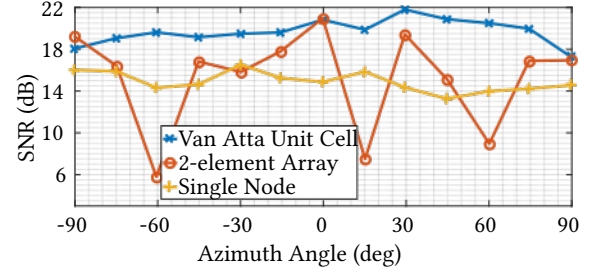
off-the-shelf hydrophone as a receiver, and a waveform generator (details in §4). We submerged the projector, hydrophone, and backscatter device underwater at a depth of 2.5 m and a fixed round-trip distance around 3 m. In each experimental trial, we rotated the backscatter device from -90° to +90° in 15° increments and computed median SNR across 625 packets at each rotation.

Fig. 9 plots the median SNR vs rotation angle for a single node (red), 2-element array (yellow), and 2-element Van Atta (blue). We make the following observations:

- The median SNR of the single node remains relatively constant around 14.5 dB across rotations. This is expected since the node itself is omnidirectional (in the horizontal plane), and the minor fluctuations (of approximately 2 dB) are due to small variations in channel conditions.
- The median SNR of the 2-element array peaks to 20 dB (at 0°) but fluctuates significantly across angles, with SNRs as low as 6 dB at certain orientations. Thus, while a simple 2-element array outperforms the single node at some angles, it significantly underperforms it at other angles, and would not be desirable in a practical system.
- Finally, the median SNR of the Van Atta unit cell remains relatively constant around 20 dB across rotations. This leads to two key conclusions: first, the Van Atta indeed outperforms the single node by around 5.5 dB, agreeing well with the maximum theoretically expected improvement over a single-node of $20 \log_{10}(N) = 6$dB for N=2. Second, it shows that unlike the standard 2-element array, the Van Atta achieves retrodirectivity as it can hold the same SNR across rotations.

3.3 From Unit Cell to 1D Van Attas

Now that we have described the basic unit cell of piezoelectric Van Atta, this section will focus on extending the unit cell Van Atta to larger structures in order to achieve higher gains and thus longer distances. Recall that the SNR gain of the Van Atta is $20 \log_{10}(N)$, where N is the number of elements in the array.[7] Fig. 11a shows the architecture of a 4-element Van Atta array. To achieve retrodirectivity, the elements are connected around an axis of symmetry realized here by choosing the inner transducers (nodes 2 and 3) as one pair, and the outer ones (nodes 1 and 4) as the other pair. Connecting each pair and switching them simultaneously using the method described in §3.1 enables retrodirectivity.

---

[5]For a detailed analysis of the power transmission and reflection waves and their effect on the operation of a piezoelectric Van Atta array, we refer the reader to Appendix A and C

[6]Note that achieving a separation of $\lambda/2$ is not feasible due to the volumetric structure of the nodes.

[7]Appendix D describes how we implemented and evaluated VABs with different N, and demonstrates that SNR and BER improve with larger N.
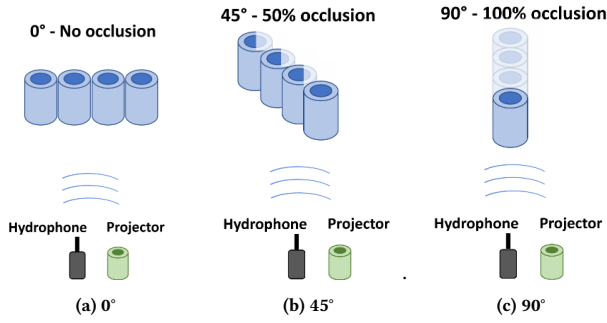
Figure 10: Occlusion Problem in 1D arrays. (a) An array 0° with respect to the projector-hydrophone pair does not suffer from occlusion. (b) at 45°, the array suffers from around 50% occlusion due to physical blockage from other nodes (c) The occlusion worsens to 100% at 90°.

While extending the Van Atta array beyond 2 elements provides an SNR gain proportional to the number of elements, a Van Atta array with more than 2 elements poses new challenges. Since acoustic transducers are 3D structures, rather than planar (as with RF/mm-waves Van Atta arrays), their interrogation from oblique angles may lead to blockage and diffraction by nearby nodes. This problem is shown in Fig. 10 where four elements are first placed at 0°, then rotated to 45° and 90° with respect to the projector/hydrophone. Due to their physical size, elements closer to the source begin to *occlude* the further ones. In Fig. 10a, the projector and hydrophone have a direct line-of-sight to all elements. However, in Fig. 10b, when the array is at a 45° rotation with respect to the hydrophone-projector pair, about 50% of each of the nodes (aside from the nearest one) are occluded. This reduces the amount of power delivered to occluded nodes and becomes most problematic when the array is at 90° rotation as in Fig. 10c. Here, almost all the nodes aside from the first are blocked. This significantly impacts the performance of the Van Atta array and prevents it from achieving the expected gains at large angles. Addressing this problem is important since in practical deployments one may not know where the backscatter array is deployed, or the projector/hydrophone may be mounted on a mobile drone whose orientation is bound to change with respect to the array as it travels.

Staggered Architecture: To overcome this problem, we *staggered* the elements of the array by placing them at different heights. Such an approach allows interrogating signals to reach all the elements at all rotations while minimizing occlusions, thus bringing the gain of the Van Atta across all orientations. Fig. 11b illustrates the approach to staggering for a 4-element Van Atta array, where two nodes in the same pair are placed at different levels. While this architecture does not completely remove the occlusion problem, it significantly alleviates it, allowing for acoustic power to always have a direct line of sight to at least two elements, instead of one.

To evaluate the impact of staggering, we performed an experiment to compare the staggered and non-staggered architectures for a 4-element Van Atta array by rotating both arrays from -90° to +90° in steps of 15° and measuring the SNRs at each angle. In the experiment, the projector, hydrophone, and backscatter device are 2.5 m deep in water. We sent 625 packets of 24 bits each and computed the median SNR for each architecture at each angle.

Fig. 12 illustrates the results of this experiment plotting the staggered architecture (in red) and the non-staggered (in blue). The figure shows that without staggering, the 4-element Van Atta array experiences a significant drop in the channel SNR of more than 6 dB beyond 60°. This is due to the occlusion problem described earlier. However, with the implementation of staggering in the 4-element array, the SNR at -90°, -75°, +75°, and +90° is larger by at least 4 dB and at most 9 dB, significantly improving the SNR at large incidence angles. Therefore, by staggering the Van Atta array elements, we overcame the occlusion problem and achieved orientation-agnostic retrodirective piezoacoustic backscatter.

3.4 From 1D to 2D Van Attas

To further increase the gain and range of our VAB architecture, we need to add more elements to our design. One approach to achieve this is to continue expanding the array along the same line (i.e., by adding more elements horizontally). However, doing so would compromise the gain of the array at nearby distances. This is because the larger an array is in any dimension, the further one needs to be from it in order to achieve the far-field properties for array gain [30, 37].

A more ideal approach to increase the gain is to stack new elements in multiple rows, thus creating a 2D array. Not only would this new architecture offer additional gain ($20 \log_{10}(N)$ with N number of elements in the array [37]), but it would also enable retrodirectivity in both azimuth and elevation planes while maintaining a compact form factor. Interestingly, while a 1D Van Atta is composed of an array of elements interconnected in symmetrical pairs with reference to an *axis* of symmetry, as shown previously in Fig. 11a , the 2D array rather requires a *center* of symmetry, as shown in Fig. 11c with the 4x2 Van Atta array.

The design of a 2D array carries similar challenges to those of a 1D array but in both planes. Similar to how increasing the number of elements in one axis could lead to occlusion and thus hinders the performance of the Van Atta at oblique angles, the addition of more rows would result in the same problem with a wave interrogating the array from above or below. Therefore, to mitigate this problem, we staggered the elements of the array in both dimensions (as we show in §4). A micro-benchmark empirically demonstrating this 3D retrodirectivity is provided in Appendix E.

3.5 From Van Atta Nodes to Networks

Building on the core VAB node architecture, we can design an entire VAB underwater backscatter network.

Backscatter Communication. Recall from §2 that an underwater backscatter node communicates information by modulating the incoming acoustic signal. Similar to previous backscatter systems [3, 21, 29], VAB adopts FM0 modulation on the uplink. The uplink data from the Van Atta node is packetized such that the payload is preceded by a preamble which is later used for detection and equalization. The FM0-encoded backscatter signal from the Van Atta node is received and decoded by a hydrophone array.

Decoding. To deal with the dispersive underwater channel, we adopt an adaptive multi-channel decision feedback equalizer (DFE) built on past work in underwater acoustic communications to optimally combine received signals across multiple hydrophones [25].

(a) 1D Van Atta Array **(b) Staggered Architecture.** **(c) 2D Van Atta Array**
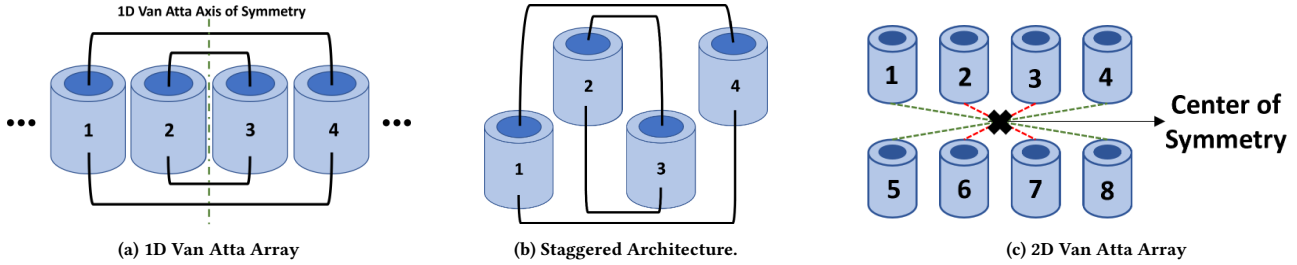
Figure 11: Multi-node Van Atta architectures. (a) 4-element Van Atta where pairs are connected around symmetry axis. (b) The architecture creates a difference in elevation between the elements in a pair of the Van Atta. (c) A 4x2 architecture, where elements are connected around a center of symmetry.
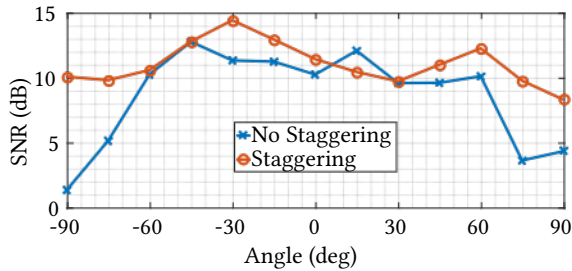
Figure 12: SNR vs. Angle. The channel SNR (dB) plotted vs. azimuth angle of the non-staggered (blue) and the staggered (red) 4x1 Van Atta arrays.

To continually track the channel variations, we perform per-symbol RLS update on the coefficient vector , which minimizes the following minimum-squared-error (MSE) cost function:

$$J_i(c) \quad \sum_{l\ 0}^{i} \lambda^{i\ l} |o_l \quad d_l|^2$$

where o_l represents the equalized symbol, $\mathbf{d}_l$ represents the equalization decision, λ denotes the forgetting factor. The above optimization can be solved with the classical Wiener's normal equation [25]. Since past underwater DFEs were designed for standard phase-shift keying (e.g., BPSK), we adapted them to FM0-encoded data by treating the FM0 coding of data rate f_d as minimum-shift keying (MSK) with f_{c0} $\pm 0.75 f_d$ constant subcarrier. Appendix H provides the mathematical analysis for this pre-processing.

4 IMPLEMENTATION EVALUATION

4.1 Van Atta Array

The Van Atta array architecture includes underwater transducers, transformer-based matching networks for each individual element of the array, and a switching mechanism.

(a) Underwater Transducers. At the core of the transducer is the SMC5447T40111 piezoceramic cylinder from Steminc [38], with a nominal resonance frequency of 17 kHz in radial mode. To fabricate the transducer, we followed a similar process to past work [3], modifying the procedures to improve ruggedization and waterproofing. Appendix F details our transducer design and fabrication process.

(b) Array. We implemented Van Atta structures of different sizes by combining two, four, and eight transducers in different organizations: linear, 2D, staggered, etc. For brevity, we describe our most

comprehensive 8-element array, which we denote *4x2 staggered Van Atta array* and which we use in most of our evaluation. As shown in Fig. 13a, the array consists of two rows of four elements each and the elements are placed in a staggered configuration to overcome the occlusion problem. We implemented other arrays either as a subset or simplified variant of this design and describe them whenever they are used. In our evaluation, the Van Atta array is entirely submerged in water.

It is worth noting that the elements in our arrays are spaced at about one wavelength due to volumetric constraints, since the node itself has a diameter of about one λ. In the absence of such constraint, one would space the nodes at $\lambda/2$. Interestingly, our chosen spacing of λ still generates the same power density in the direction of the source and does not impact the operation (or benefits) of the Van Atta. This is because the increased spacing creates new *additional* grating lobes but with narrower beams [39]. Thus, the main lobe (while being narrower due to the wider aperture) maintains the same power in the retrodirective direction.

(c) Hardware. We custom-designed and fabricated a printed circuit board (PCB) for backscatter modulation/control and impedance matching (photo shown in Fig. 24b of Appendix F). Impedance matching is implemented as a transformer-based network as described in §3.1. For the transformer core, we use an RM-6 ferrite core with A_L 250 nH [40], providing 250 nH per turn squared. The backscatter nodes are approximately 50 $j220\Omega$, yielding N_p 90 turns on the primary (the port connected to the backscatter node) and N_s 26 turns on the secondary (the port that the switching network sees), fully matching end-to-end the node to a real impedance of 50 Ω.

Backscatter switching is realized using eight TS5A2316 2-channel analog switching ICs [41]. The IC network is designed to enable two modes of operation: 1) our cross-polarity switching for retrodirective backscatter (described in §3.1); 2) standard array-based switching. The switches can be controlled using any processor (e.g., micro-controllers); for simplicity, we use an N210 USRP software radio [42]. [8]
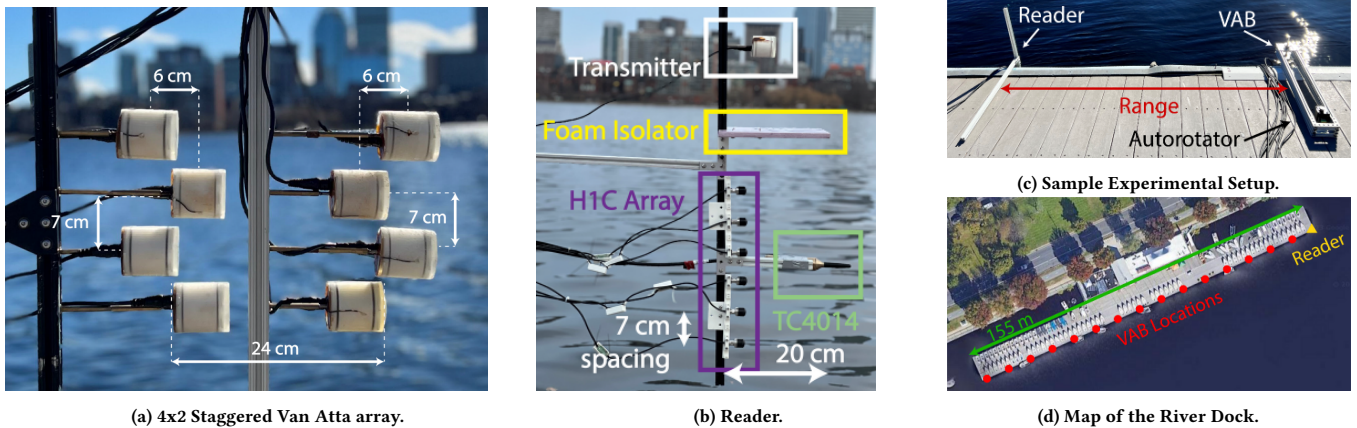
4.2 Reader Implementation

Our reader consists of two main components:

(a) Transmitter. We use an underwater transducer (described in §4.1) as our transmitter. The transmitter node is connected to a class-D power amplifier TI TPA3245 [43] through a high-power

---

[8]More details on the PCB and power consumption are in Appendix F.

(a) 4x2 Staggered Van Atta array.　(b) Reader.　(c) Sample Experimental Setup.　(d) Map of the River Dock.

Figure 13: System Implementation and Evaluation. (a) The 4x2 staggered Van Atta array. (b) Our reader includes a transmitter and hydrophone array. (c) shows a sample testing at close-by range, where the reader is on the left and the backscatter array and supporting hardware are on the right. (d) shows an overhead view of the dock used for evaluation, marking sample locations where the experiments were conducted.

transformer matching network with the same core as in §4.1. The transformer is designed using the same primary magnetizing inductance as in Eq. 5 while adjusting the secondary turns to achieve 4Ω impedance to maximize power transfer from the audio power amplifier. The input signal to the power amplifier is generated by a high-resolution audio DAC ESS ES9018[44]. To reduce the noise leakage at the co-located receiver array, we insert a foam board (XPS [45] 30x30x1.3 cm^3) between the hydrophone array and the projector as shown in Fig. 13b in order to reflect the majority of the line-of-sight leakage path from the projector. Throughout our evaluation, we transmitted at 18.5 kHz using 1.8 watts (or less) of input electrical power unless otherwise specified.[9]

(b) Receiver array. The backscattered signal is received by a 7-element receiver array shown in Fig. 13b, which consists of a Reson TC4014 hydrophone and 6 low-cost Aquarian Audio H1C hydrophones [47, 48]. Each H1C hydrophone is connected to a 30dB custom-designed amplifier based on Analog Device AD8656 [49, 50]. The received signal at each hydrophone is sampled by a 24-bit ADC Cirrus Logic CS5381 [51]. For the digital interface, the ADCs for reception and the DAC for transmission are connected to a Xilinx 7A200T FPGA [52] in a custom PCB board that translates between SPI serial data and PCIe bus attached to a computer that runs the data recording and offline decoding pipeline.

4.3 Evaluation

(a) Testing Environment. We evaluated VAB in both a river (4 m depth) and the Atlantic ocean (30 m depth). Most experiments were performed in the river. Our evaluation environments had standard sources of underwater noise and interference, including marine animals, motorboats, sailboats, and ships, as well as other underwater acoustic communication systems. At the river, we evaluated VAB with our equipment on a dock that is about 155 m in length, and as such our practical range limit is 155 m one-way (and 310 m

---

[9]Our transmitted cumulative source exposure level (SEL_{cum}) in each experiment was in compliance with the limits defined by the marine mammal protection act (MMPA) [46].

round-trip). An example setup of the dock can be seen in Fig. 13c and an overhead view of our evaluation environment at the dock is shown in Fig. 13d. In our experiments, we varied the location, depth, and orientation of the transmitter, receiver, and backscatter nodes. Sample evaluation locations are marked by red dots in Fig. 13d. Our experiments were performed across different weather conditions (including wind, rain, and snow).

(b) Rotations. To evaluate the angular coverage of various VAB implementations, we built a custom rotating device that uses an STM23IP-2EN NEMA 23 stepper motor [53] and a belt drive to rotate a shaft that the backscatter device is attached to in the water. This device, which we refer to as the "autorotator" (photo in Fig. 24c of Appendix F), allows us to achieve an angular precision of ∼1°.

(c) Metrics and Uplink Data. We evaluated both the bit-error rate (BER) and the signal-to-noise ratio (SNR) in our results. We compute BER by calculating the ratio of incorrectly decoded bits to the number of known transmitted bits, and SNR by calculating the ratio of the magnitude squared of the output symbol estimate to the mean square error over the output estimated bits from the DFE, as defined in prior work on underwater communication systems [25]. We set the minimum BER to 10^{-4} since our packet size is always smaller than 10^4 bits.

5 RESULTS

This section reports how we evaluated the performance of VAB across communication range, throughput, and the number of hydrophone channels used in decoding the received backscatter signal. We performed over 1,500 experimental trials in total.

5.1 Communication Range

First, we evaluated the communication range of VAB by backscattering data at varying ranges. We compared the 4x2 staggered Van Atta array to two additional implementations:

- **Baseline** (Omnidirectional Node, Single Channel): The baseline was designed to follow past work on underwater backscatter [3, 21]. These systems leverage a single omnidirectional

transducer for backscatter and a single-channel hydrophone receiver.[10] For fairness of comparison, we used our optimized transducer (described in §4.1) as backscatter node in this baseline, and the receiver is configured to decode from a single TC4014 hydrophone channel.

- **Enhanced Baseline** (Omnidirectional Node, Multichannel): We implemented an enhanced baseline which uses the same omnidirectional backscatter node as above, but also used our multichannel receiver (6 H1C hydrophones and 1 TC4014 hydrophone), as described in §4.2.

We performed trials across three days at distances ranging from 10 m to 150 m (the edge of our dock). In each experiment, we fixed the data rate to 500 bps and the transmit power to 1.8 W. For each of the three days, we fixed the location of the reader at one specific location, but varied this location across days in order to obtain range results in different environments. We performed 8 trials at each range for each of the three days and the three configurations, yielding a total of 1,092 experimental trials. We decode the received signal using the robust decoding pipeline described in §4.2 and compute the BER across the 24 trials at each range.

Fig. 14 plots the median BER vs. range for VAB (blue), baseline (yellow), and enhanced baseline (red). We make the following remarks:

- For the baseline, as the range increases from 10 to 20m, the BER sharply increases from 2×10^{-2} to 0.5 and then remains around 0.5 for all measured ranges, displaying an inability to decode at any distance above 20m. These results are in line with the highest ranges reported in previously published work at the corresponding throughputs [3, 5, 21].[11] The increase in BER with distance is expected since the backscatter response gets weaker with distance, and eventually drops below the noise floor, preventing decoding.
- The enhanced baseline displays a similar trend with a sharp increase in BER from 10^{-3} at 10m to 0.5 at 40m. Its improvement compared to the baseline is expected since the receiver incorporates a multichannel DFE.
- Finally, for VAB, as the distance increases from 10 to 150m, the BER increases only from 10^{-4} to 2×10^{-3}. As with the previous cases, the BER increases with range is expected due to the reduction in backscatter response with distance. But, even at 150m (i.e., 15x the distance of 10 m), VAB outperforms the baseline by more than two orders of magnitude in BER; and, it achieves a similar BER as the enhanced baseline at 15x more range (150 m vs 10 m).

These results demonstrate that VAB significantly extends the range of underwater backscatter (achieving 300 m round-trip) over state-of-the-art past systems (and their enhancements). Importantly, these BERs are for the raw data (i.e., before error-correction) and at relatively low power (1.8 W).

---

[10]Note that while [21] has higher bandwidth than [3], our evaluation focuses on a narrow bandwidth; hence, both would perform similarly within the bandwidth of operation in our evaluation.

[11]It is worth noting that the range can be boosted by applying coding and/or if the projector is closer to the backscatter node. For example, U2B achieves 60 m round-trip (i.e., 30 m one-way) by coding to birtrate of 1 bit per 120 s (see Fig. 12 in [21]). Another example is that underwater backscatter imaging [5] achieves a range of 40 m using a shorter downlink (projector-to-backscatter distance was 1 m). Applying similar levels of coding or downlink ranges is likely to extend VAB to kilometer-scale distances.
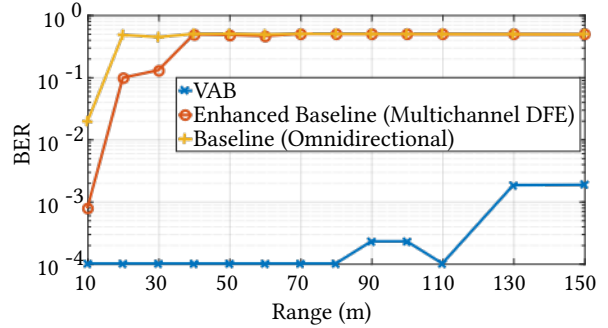

Figure 14: BER vs Range. The figure plots the BER vs range for VAB (blue), baseline (red), and enhanced baseline (yellow).

It is worth noting that the range improvement achieved by VAB (15×) exceeds what one would expect from typical Van Atta architectures, particularly in the context of past RF designs. This can be due to two reasons that stem from the nature of the underwater acoustic channel:

- First, a key challenge with decoding underwater acoustic signals arises from severe multipath caused by sound reflections off the water surface and river floor (particularly in shallow-water environments); this multipath causes inter-symbol interference (ISI) which our decision-feedback equalizer estimates and eliminates. An additional benefit of Van Atta retrodirectivity (on top of the array gain) underwater is that it mitigates this multipath (since it focuses the acoustic power back towards the transmitter causing less signal to travel on paths where reflections may occur). This reduces ISI, which in turn enables the decision feedback equalizer to better estimate the received bits and thus reduces the BER on top of the reduction in BER due to the increased signal strength from the Van Atta.
- The second reason is the spreading factor of propagation. In particular, while in free-space RF, the backscatter spreading factor is 4 ($10\log_{10}(d^4)$), in shallow underwater environments this factor is smaller and is characterized as practical spreading . On one-way links, this factor is about 1.5 instead of 2 [54, 55], thus on backscatter links the factor would be $10\log_{10}(d^3)$ instead of $10\log_{10}(d^4)$. As a result, a power gain (from arraying) yields more range improvement in our underwater acoustic environments than it would in RF environments.

5.2 Retrodirectivity

Next, we evaluated the retrodirectivity of VAB's design. Recall that a key benefit of the design is to enable backscatter irrespective of angular rotation. Thus, we compared the 4x2 staggered VAB array to a 4x2 standard array across angular rotations. To isolate the impact of angular coverage, we fixed the distance between the reader and the VAB node to 60 m. We rotated the array in the azimuth plane from -90° to +90° in steps of 5°. At each angle, we ran 6 trials of a communication test by transmitting packets of 10,000 bits at 500 bps and 1.8 W of transmit power. We repeated this experiment using the standard backscatter array for a total of 444 experimental trials, and we computed CDFs of the output SNR and BER from our decoding pipeline.
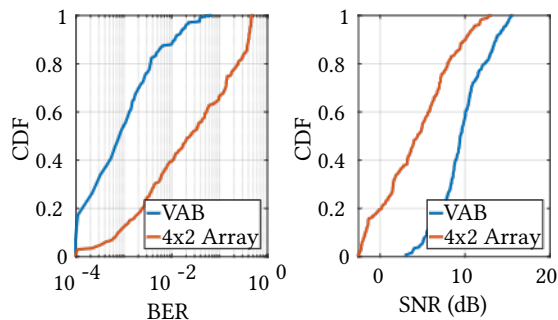
Figure 15: CDFs of BER and SNR across angle and trial. BER (left) and SNR (right) for VAB (blue) and the 4x2 standard backscatter array (red).

Fig. 15 plots the CDFs of SNR and BER for VAB (blue) and a standard backscatter array (red). We note the following:

- VAB's median and 90th percentile BER are 8.8×10^{-4} and 1.2×10^{-2} respectively, while the 4x2 array's median and 90th percentile BER are roughly 2.2×10^{-2} and 0.41 respectively. The 90th percentile BER of VAB outperforms that of the standard backscatter array, highlighting the significant performance gain achieved with retrodirectivity.
- The median SNR of VAB and the standard array is roughly 9.6 dB and 4.6 dB. Furthermore, the SNR CDF of VAB is visibly steeper than that of the standard array. The larger median and steeper curve (hence lower variance) highlight VAB's ability to maintain its performance gain across azimuth angle where the standard array cannot.

These results demonstrate VAB's remarkable ability to provide retrodirective underwater backscatter and outperform the same-sized standard array through the use of our cross-polarity switching. This shows that VAB not only significantly extends the range of state-of-the-art backscatter systems, but it does so regardless of its orientation in the water.

5.3 Performance across Bit Rate

Next, we would like to evaluate the performance of VAB across bit rate. We performed an experiment similar to §5.1 across range, but this time, we varied the bit rate using the 4x2 staggered Van Atta array as the backscatter device. We selected three bit rates, namely: 500 bps, 1 kbps, and 2 kbps. Again, we performed 8 trials at each range for each of three days, yielding 24 trials in total per bit rate at one range. We compute BER across the 24 trials at each range and bit rate.

Fig. 16 plots the median BER vs. range for three bit rates 500bps (blue), 1kpbs (red), and 2kbps (yellow).[12] We make the following remarks:

- At 500bps, VAB's BER increases from 10^{-4} at 10m to 2×10^{-3} at 150m. Likewise, similar trends are observed with 1kpbs and 2kpbs, with the BER increasing from 10^{-4} to 3×10^{-3} and 7×10^{-2}, respectively. The general trend of increasing BER with increasing distance irrespective of the throughput is expected and is due to the drop in the SNR at larger distances. The small variations in BER at any given throughput are due to channel variations both

with time and with location in which the transmitter, receiver, and backscatter device.
- At 100m, the BER increases from 2×10^{-4} at 500bps, to 6×10^{-4} at 1kbps, and up to 6×10^{-3} at 2kpbs. This BER increase at any given range as the throughput increases is expected since a higher throughput spreads the backscatter signal over a wider bandwidth, thus reducing the overall SNR across that bandwidth.[13] Nonetheless, even at 2 kbps, VAB can correctly decode packets, far beyond what the baselines could at 500 bps and much smaller ranges.

5.4 Performance across Transmitted Power

Next, we evaluate the effect of the reader's transmitted power on VAB. Specifically, even though the backscatter node (or VAB) itself consumes the same amount of power, the overall system performance depends on the amount of power transmitted by the reader. Since a higher transmitted power would result in a higher backscattered power, we expect to see a higher SNR at the receiver and thus improved performance. We compared the performance across range for two different power levels: the first is 1.8 W similar to §5.1, and the second is 0.11 W. We performed 8 trials at 500 bps at each range from 10 m to 150 m across three days. We computed the BER across the 24 trials at each range.

Fig. 17 plots the median BER vs. range for VAB at 0.11 W (blue) with the result obtained for 1.8 W (red) in §5.1.[14] We make the following remarks:

- The BER obtained with VAB using 0.11 W of transmitted power increases from 10^{-4} at 10m to 0.1 at 150m. This increase in BER with the range is expected for the same reasons described earlier.
- A similar trend is observed with 1.8 W of transmitted power with a BER increase from 10^{-4} to 2×10^{-3}. However, VAB at 0.11 W displays a BER that is one order of magnitude higher than that using 1.8 W of transmitted power. This is expected since the power of backscatter response is directly proportional to the reader's transmit power (as the node is merely reflecting it), and a lower power results in lower SNR (and thus higher BER).
- As described previously, the small variations in BER with range for any transmitted power are due to the time and location varying channel response on any given day.

5.5 Performance vs Hydrophone Channels

Our final result aimed to evaluate the impact of the number of hydrophone channels at the receiver on the overall system performance. To this end, we used the same received signals from §5.1 (i.e., 4x2 staggered Van Atta array vs range at 500bps and 1.8 W) but processed the data by varying the number of receiver channels. Specifically, for each experimental trial, we used our robust multi-channel DFE decoder but on a different number of channels. For completeness, used every possible combination of $N = 1, 2, 3, 4, 5, 6, 7$ hydrophone channels in generating these results. Specifically, for any number of selected receive channels N, we generate $\binom{7}{N}$ unique combinations of receive channels to use in the decoding pipeline and compute CDFs of the selected $\binom{7}{N}$ combinations for each of

---

[12]Additional results for the enhanced baseline are in Appendix G.

[13]Assuming an AWGN channel, the overall noise power is directly proportional to the bandwidth [56].

[14]Additional results for the enhanced baseline are in Appendix G.
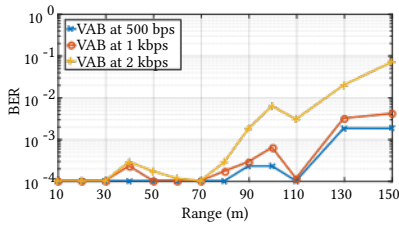
Figure 16: BER vs. Range for different bit rates. This figure plots the BER performance vs range of the 4x2 staggered VAB for 500 bps (blue), 1 kbps (red), and 2 kbps (yellow).
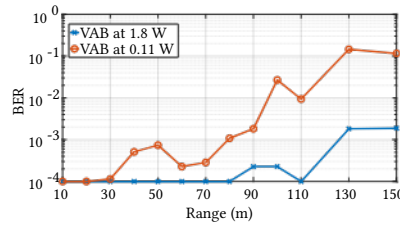
Figure 17: BER vs. Range for different transmitted powers. The figure plots the BER vs range performance of the 4x2 staggered VAB for 1.8 W (blue) and 0.11 W (red).
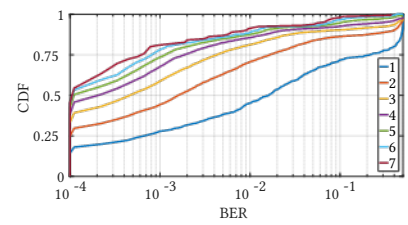
Figure 18: CDFs of BER for each of N 1, 2, 3, 4, 5, 6, 7 hydrophone channels. Each of these CDFs is generated using the 4x2 Van Atta array data at 500 bps with 1.8 W of transmit power.

the 24 trials at each range.

The CDFs of BER for each number of selected receive channels N 1, 2, 3, 4, 5, 6, 7 are plotted in Fig. 18. We make the following observations:

- VAB's median and 90th percentile BER decrease from 1.5×10^{-2} and 0.5 to 10^{-4} and 10^{-2}, respectively with the increase of hydrophone channels from 1 to 7. This is expected since using multiple channels provides a gain in received power and spatial diversity.
- The median BER for the 7-channel decoder is roughly 10^{-4}, and more than 75% of all trials at all ranges achieve a BER of 10^{-3} or lower. This highlights the ability of VAB to perform well across a wide variety of channel responses up to 150 m in range.

6 DISCUSSION CONCLUSION

This paper introduces VAB, a technology for retrodirective underwater backscatter, which enables ultra-low-power longer-range networking in underwater environments. Our evaluation demonstrates that VAB achieves orders of magnitude longer communication ranges than state-of-the-art underwater backscatter solutions at standard underwater throughputs and relatively low reader transmit power (around 1.8 W), noting that the backscatter node itself remains net-zero power.[15] As the research evolves, it is desirable to extend it in multiple ways:

- **Range:** The realized range can be extended by applying various techniques such as coding or even by transmitting higher powers (for example, underwater SONARs can transmit up to tens of kWatts of power to operate over long ranges [57]).
- **Mobility:** While our evaluation was performed across different weather conditions (including snow/rain/wind), our system was primarily tested in stationary setups, which would be typical for coastal deployments or even low-mobility environments. As the research evolves, it would be interesting to extend these designs to mobile environments, such as underwater drones, surface vessels, or even by attaching the sensors to marine animals. It is worth noting that retrodirective architectures are beneficial with or without mobility, but they can bring even more benefits under mobility (since they are orientation agnostic).
- **Depth:** Our evaluation was performed at shallow-depth environments (at a depth of around 3 m). These environments

present particular challenges due to severe multipath. It would be interesting to extend our systems to operate at greater depth. While our VAB architecture should, in principle, maintain its retrodirective gains at any depth, developing a system that can operate at greater depth requires hardening the backscatter transducers and hardware to withstand the higher pressure (and lower temperature) of deep-sea environments.

- **Large Scale Networking:** While our implementation in this paper evaluated multiple proof-of-concept VAB prototypes (with different shapes and sizes), this evaluation primarily focused on the performance of an individual node as a function of different parameters. As the research evolves, it would be valuable to extend our design to larger networks of nodes, for example by combining it with past work on underwater backscatter networks [3, 21] and extending the base station with higher-layer protocols for beamsteering, medium access control, etc.

While many exciting problems remain open, this research marks an important step towards an energy-autonomous ocean IoT and its various applications in climate and ecological monitoring, weather prediction, scientific exploration, food production, and more.

ACKNOWLEDGMENTS

REFERENCES

[1] Rajeswari Jayaraman. Beyond IoT: Internet of Underwater Things to Network the Oceans. https://www.prescouter.com/2017/06/internet-of-underwater-things/, 2017.

[2] Chien-Chi Kao, Yi-Shan Lin, Geng-De Wu, and Chun-Ju Huang. A comprehensive study on the internet of underwater things: applications, challenges, and channel models. *Sensors*, 17(7):1477, 2017.

[3] Junsu Jang and Fadel Adib. Underwater backscatter networking. In *Proceedings of the ACM Special Interest Group on Data Communication*, pages 187–199, 2019.

[4] En-Cheng Liou, Chien-Chi Kao, Ching-Hao Chang, Yi-Shan Lin, and Chun-Ju Huang. Internet of underwater things: Challenges and routing protocols. In *2018 IEEE International Conference on Applied System Invention ICASI*, pages 1171–1174. IEEE, 2018.

[5] Sayed Saad Afzal, Waleed Akbar, Osvy Rodriguez, Mario Doumet, Unsoo Ha, Reza Ghaffarivardavagh, and Fadel Adib. Battery-free wireless imaging of underwater environments. *Nature communications*, 13(1):1–9, 2022.

---

[15]Recall that backscatter is net-zero power because the backscatter node does not generate its acoustic signal but communicates by simply modulating the reflection of an external acoustic signal.

[6] Michael H Carr, Michael JS Belton, Clark R Chapman, Merton E Davies, Paul Geissler, Richard Greenberg, Alfred S McEwen, Bruce R Tufts, Ronald Greeley, Robert Sullivan, et al. Evidence for a subsurface ocean on europa. *Nature*, 391(6665):363–365, 1998.

[7] Kakani Katija, Rob E Sherlock, Alana D Sherman, and Bruce H Robison. New technology reveals the role of giant larvaceans in oceanic carbon cycling. *Science Advances*, 3(5):e1602374, 2017.

[8] Camilo Mora, Derek P Tittensor, Sina Adl, Alastair GB Simpson, and Boris Worm. How many species are there on earth and in the ocean? *PLoS biology*, 9(8):e1001127, 2011.

[9] Sustainable fisheries and aquaculture for food security and nutrition. https://www.fao.org/3/i3844e/i3844e.pdf.

[10] Dana R Yoerger, Annette F Govindarajan, Jonathan C Howland, Joel K Llopiz, Peter H Wiebe, Molly Curran, Justin Fujii, Daniel Gomez-Ibanez, Kakani Katija, Bruce H Robison, et al. A hybrid underwater robot for multidisciplinary investigation of the ocean twilight zone. *Science Robotics*, 6(55):eabe1901, 2021.

[11] Jeff Tollefson. Sensor array provides new look at global ocean current. Nature, 2018.

[12] Stephen C Riser, Howard J Freeland, Dean Roemmich, Susan Wijffels, Ariel Troisi, Mathieu Belbéoch, Denis Gilbert, Jianping Xu, Sylvie Pouliquen, Ann Thresher, et al. Fifteen years of ocean observations with the global argo array. *Nature Climate Change*, 6(2):145–153, 2016.

[13] Philip J. Bresnahan, Elizabeth Farquhar, Daniel Portelli, Michael Tydings, Taylor Wirth, and Todd Martz. A low-cost carbon dioxide monitoring system for coastal and estuarine sensor networks. *Oceanography*, 2023.

[14] ARPA-E. SEA-CO2: Sensing Exports of Anthropogenic Carbon through Ocean Observation. https://arpa-e.energy.gov/sites/default/files/inline-files/ARPA-ESlide-SimonandDan_0.pdf.

[15] USGS. USGS Installs Storm-Tide Sensors Along Gulf Coat for Hurricane Nate. https://www.usgs.gov/news/national-news-release/usgs-installs-storm-tide-sensors-along-gulf-coast-hurricane-nate.

[16] Tidal X. Protecting the ocean with technology systems while feeding humanity sustainably. https://x.company/projects/tidal/.

[17] DARPA. Ocean of Things Aims to Expand Maritime Awareness across Open Seas. https://www.darpa.mil/news-events/2017-12-06, 2017.

[18] NSF Beta. NSF's Convergence Accelerator invests $30 million to tackle challenges related to the blue economy. https://beta.nsf.gov/news/nsfs-convergence-accelerator-invests-30-million.

[19] Axios. New ocean tech fund makes waves. https://www.axios.com/2022/10/20/propeller-ocean-tech-venture-fund.

[20] Tech Funding News. London-based blue economy focussed VC totals €130M to invest in tech startups saving marine ecosystems. https://techfundingnews.com/london-based-blue-economy-focussed-vc-totals-e130m-to-invest-in-tech-startups-saving-marine-ecosystems/.

[21] Reza Ghaffarivardavagh, Sayed Afzal, Osvy Rodriguez, and Fadel Adib. Ultra-wideband underwater backscatter via piezoelectric metamaterials. In *Proceedings of the ACM Special Interest Group on Data Communication*, 2020.

[22] Lester Clare Van Atta. Electromagnetic reflector, Oct 1959. Patent No. US-2908002-A, Filed June 8th, 1955, Issued Oct. 9th, 1959.

[23] Mohammad Hossein Mazaheri, Alex Chen, and Omid Abari. mmtag: a millimeter wave backscatter network. In *Proceedings of the 2021 ACM SIGCOMM 2021 Conference*, pages 463–474, 2021.

[24] Elahe Soltanaghaei, Akarsh Prabhakara, Artur Balanuta, Matthew Anderson, Jan M Rabaey, Swarun Kumar, and Anthony Rowe. Millimetro: mmwave retro-reflective tags for accurate, long range localization. In *Proceedings of the 27th Annual International Conference on Mobile Computing and Networking*, pages 69–82, 2021.

[25] Milica Stojanovic, Josko Catipovic, and John G Proakis. Adaptive multichannel combining and equalization for underwater acoustic communications. *The Journal of the Acoustical Society of America*, 94(3):1621–1631, 1993.

[26] Lee Freitag, Matthew Grund, Sandipa Singh, James Partan, Peter Koski, and Keenan Ball. The whoi micro-modem: An acoustic communications and navigation system for multiple platforms. In *Proceedings of OCEANS 2005 MTS/IEEE*, pages 1086–1092. IEEE, 2005.

[27] Sayed Afzal, Reza Ghaffarivardavagh, Osvy Rodriguez, and Fadel Adib. Enabling higher-order modulation for underwater backscatter communication. In *Proceedings of the MTS/IEEE OCEANS Conference*, 2020.

[28] Reza Ghaffarivardavagh, Sayed Saad Afzal, Osvy Rodriguez, and Fadel Adib. Underwater backscatter localization: Toward a battery-free underwater gps. In *Proceedings of the 19th ACM Workshop on Hot Topics in Networks*, HotNets '20, page 125–131, New York, NY, USA, 2020. Association for Computing Machinery.

[29] Sayed Saad Afzal, Waleed Akbar, Osvy Rodriguez, Mario Doumet, Unsoo Ha, Reza Ghaffarivardavagh, and Fadel Adib. Battery-free wireless imaging of underwater environments. *Nature Communications*, 13(1):5546, Sep 2022.

[30] Charles H Sherman and John L Butler. *Transducers and arrays for underwater sound*, volume 4. Springer, 2007.

[31] E Sharp and M Diab. Van atta reflector array. *IRE Transactions on Antennas and Propagation*, 8(4):436–438, 1960.

[32] Jimmy G. D. Hester and Manos M. Tentzeris. Inkjet-printed flexible mm-wave vanatta reflectarrays: A solution for ultralong-range dense multitag and multisensing chipless rfid implementations for iot smart skins. *IEEE Transactions on Microwave Theory and Techniques*, 64(12):4763–4773, 2016.

[33] Aline Eid, Jimmy GD Hester, and Manos M Tentzeris. Rotman lens-based wide angular coverage and high-gain semipassive architecture for ultralong range mm-wave rfids. *IEEE Antennas and Wireless Propagation Letters*, 19(11):1943–1947, 2020.

[34] Prakhar Srivastava, Brendan Nichols, and Karim G Sabra. Passive underwater acoustic markers using bragg backscattering. *The Journal of the Acoustical Society of America*, 142(6):EL573–EL578, 2017.

[35] Lester Clare Van Atta. Underwater sound reflector, Jun 1958. Patent No. US-2839735-A, Filed June 8th, 1955, Issued Jun. 17th, 1958.

[36] Texas Instruments. TS5A23160 data sheet, product information and support | TI.com. https://www.ti.com/product/TS5A23160.

[37] C.A. Balanis. *Antenna Theory: Analysis and Design*. Wiley, 2015.

[38] Steminc Piezo Ceramic Cylinder 54.1x47x40mm 17 KHz. https://www.steminc.com/PZT/en/piezo-ceramic-cylinder-541x47x40mm-17-khz.

[39] Jue Wang, Deepak Vasisht, and Dina Katabi. Rf-idraw: virtual touch screen in the air using rf signals. In *ACM SIGCOMM*, 2015.

[40] TDK RM6 ferrite core. https://www.tdk-electronics.tdk.com/inf/80/db/fer/rm_6.pdf.

[41] TI TSA5A23166 IC. https://www.ti.com/product/TS5A23166?qgpn=ts5a23166.

[42] usrp n210. http://www.ettus.com, 2018. ettus inc.

[43] TI tpa3245 power amplifier. https://www.ti.com/lit/gpn/tpa3245.

[44] ESS ES9018 DAC chip. https://www.esstech.com/wp-content/uploads/2021/02/ES9018S_Datasheet_v2.2.pdf.

[45] Owens Corning XPS material. https://www.owenscorning.com/en-us/insulation/products/foamular-250.

[46] Joe Roman, Irit Altman, Meagan M Dunphy-Daly, Caitlin Campbell, Michael Jasny, and Andrew J Read. The marine mammal protection act at 40: status, recovery, and future of us marine mammals. *Annals of the New York Academy of Sciences*, 1286(1):29–49, 2013.

[47] Reson TC4014 Hydrophone. http://www.teledynemarine.com/reson-tc-4014.

[48] H1C Hydrophone. https://www.aquarianaudio.com/h1c-hydrophone.html.

[49] AD8656. https://www.analog.com/media/en/technical-documentation/data-sheets/AD8655_8656.pdf.

[50] LT1113 (with Hydrophone amplifier schematic). https://www.analog.com/media/en/technical-documentation/data-sheets/1113fc.pdf.

[51] CS5381 ADC chip. https://www.cirrus.com/products/cs5381/.

[52] Xilinx 7a200t Core board. https://alinx.com/en/detail/301.

[53] STM23IP-2EN - NEMA 23 Integrated Drive+Motor w/ EtherNet/IP. https://www.applied-motion.com/products/integrated-steppers/stm23ip-2en. STM23IP-2EN.

[54] Andrej Stefanov and Milica Stojanovic. Communication theoretic analysis of underwater ad-hoc networks in the presence of interference. In *2010 IEEE Globecom Workshops*, pages 186–190. IEEE, 2010.

[55] Y Lysanov and LM Brekhovskikh. *Fundamentals of ocean acoustics*, volume 8. Springer, 1982.

[56] David Tse and Pramod Viswanath. *Fundamentals of wireless communication*. Cambridge university press, 2005.

[57] Robert C Gisiner. Workshop on the effects of anthropogenic noise in the marine environment, 10-12 february 1998. proceedings. Technical report, OFFICE OF NAVAL RESEARCH ARLINGTON VA MARINE MAMMAL AND BIOLOGICAL …, 1998.

[58] K. Kurokawa. Power waves and the scattering matrix. *IEEE Transactions on Microwave Theory and Techniques*, 13(2):194–202, 1965.

[59] Micro-con-X 2-pin Connector. https://www.switchcraft.com/micro-con-x-connectors-0-530-od/microconx/.

[60] clear coat low-viscosity epoxy-sealer. https://www.systemthree.com/products/clear-coat-low-viscosity-epoxy-sealer.

[61] 3M Scotchkote Electrical Coating FD. https://www.3m.com/3M/en_US/p/d/b40046251/.

[62] Jun Tan and Gordon L Stuber. Frequency-domain equalization for continuous phase modulation. *IEEE Transactions on Wireless Communications*, 4(5):2479–2490, 2005.

[63] John G.. Proakis and Masoud Salehi. *Digital communications*. McGraw-Hill., 2008.
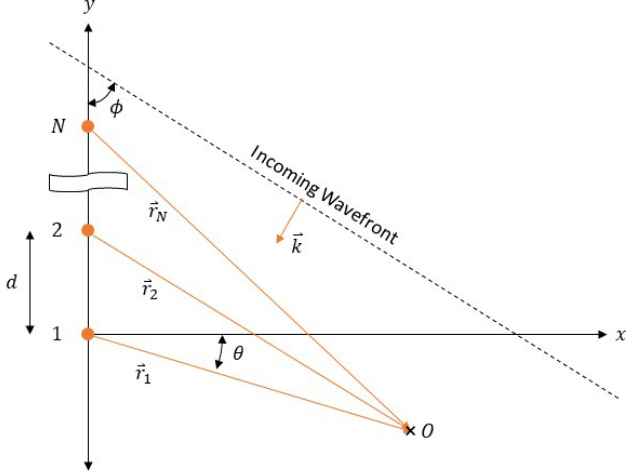
A VAN ATTA RADIATION PATTERN

Figure 19: Geometric model of Van Atta array in 2D space

The piezoelectric nodes are modeled as omnidirectional point sources in a 2D plane. There are N nodes placed uniformly on the y-axis with spacing d, with the first element centered at $(0,0)$. Only even N are considered. As shown in Fig. 19 above, the incoming wave is assumed to be planar and has wavevector $\vec{k}$. The angle of incidence is defined as ϕ and is measured from the y-axis to the plane of constant phase (the wavefront). ϕ is positive if the plane wave arrives from above the x-axis and negative if the plane wave arrives from below the x-axis. O is the point of observation of the redirected wave, and $\vec{r_n}$ is the observation vector from element n to observation point O. The derived redirected beam pattern will be computed using $\vec{r_1}$ as the observation vector in polar coordinates. θ is the angle to the x-axis of the observation vector and is positive above the x-axis and negative below the x-axis.

The incoming plane wave can be modeled as

$$a = Ae^{j(k_x x + k_y y)} \tag{6}$$

where k_x and k_y for the wavefront shown in Fig. 19 are negative and are the cartesian vector components of $\vec{k}$. We also know that

$$k_x = |\vec{k}|\cos\phi \tag{7}$$

$$k_y = |\vec{k}|\sin\phi \tag{8}$$

$$\phi = \arctan\frac{k_y}{k_x} \tag{9}$$

The Van Atta array is configured such that power incident upon node n is transferred to node $N+1-n$, and vice versa. This is achieved through a direct electrical connection between the terminals of node n and $N+1-n$ or through an electrical matching network.

We define the wave emitted from node n at node n as b_{tn}. We can then write

$$b_{tn}(\phi) = s_{nn}a\Big|_{x=0, y=(n-1)d} + s_{n,N+1-n}a\Big|_{x=0, y=(N-n)d}$$
$$= s_{nn}Ae^{jk_y(n-1)d} + s_{n,N+1-n}Ae^{jk_y(N-n)d}$$
$$= A(s_{nn}e^{-jk\sin\phi(n-1)d} + s_{n,N+1-n}e^{-jk\sin\phi(N-n)d}) \tag{10}$$

Where $k = |\vec{k}|$, s_{nn} is the reflection coefficient at node n from node n, and $s_{n,N+1-n}$ is the transmission coefficient from node $N+1-n$ to node n. The first component of the sum is the reflected wave from node n, and the second component is the transmitted wave from node $N+1-n$ to node n.

We note that at observation point O the emitted waves from each node must advance in phase by the distance given by $r_n = |\vec{r_n}|$. To compute the radiation pattern under the far field assumption, we can say that all $\vec{r_n}$ are approximately parallel and that their lengths r_n are approximately

$$r_n = r_1 - (n-1)d\sin\theta \tag{11}$$

Thus the far field wave emitted from node n at point O can be expressed as

$$b_n(r_1, \theta, \phi) = b_{tn}(\phi)e^{jkr_n}$$
$$= b_{tn}(\phi)e^{jkr_1}e^{-jk(n-1)d\sin\theta} \tag{12}$$

And the total far field wave in polar coordinates with $r = r_1$ and ϕ as an argument is

$$b(r, \theta, \phi) = \sum_{n=1}^{N} b_n(r, \theta, \phi) \tag{13}$$

Assuming that s_{nn} are equivalent for all n, $s_{n,N+1-n}$ are equivalent for all n, and applying geometric series formulas, the total far field magnitude $|b|$ can be shown to be

$$|b(r, \theta, \phi)| = A|s_{nn}\frac{\sin(N\psi'/2)}{\sin(\psi'/2)} + s_{n,N+1-n}\frac{\sin(N\psi/2)}{\sin(\psi/2)}| \tag{14}$$

where $\psi = kd(\sin\theta - \sin\phi)$ and $\psi' = kd(\sin\theta + \sin\phi)$. This pattern is independent of r and of the form of the sum of two $sinc$-like functions. The ideal Van Atta array would have $s_{nn} = 0$ and $s_{n,N+1-n} = 1$, which when substituted into $|b|$ yields

$$|b(r, \theta, \phi)| = A|\frac{\sin(N\psi/2)}{\sin(\psi/2)}| \tag{15}$$

Note that even if $s_{n,N+1-n}$ has magnitude 1 and an arbitrary phase, the magnitude pattern is equivalent to the case where $s_{n,N+1-n}$ does not have a phase, indicating that as long as the electrical network connecting nodes is lossless, matched, and reciprocal, any phase the network incurs on the signal does not change the magnitude pattern. We can check for retrodirectivity by setting $\phi = \theta$, or looking at the pattern in the direction that the original wavefront came from. This means that $\psi = 0$ and the pattern magnitude value is

$$|b(r, \theta, \theta)| = AN \tag{16}$$
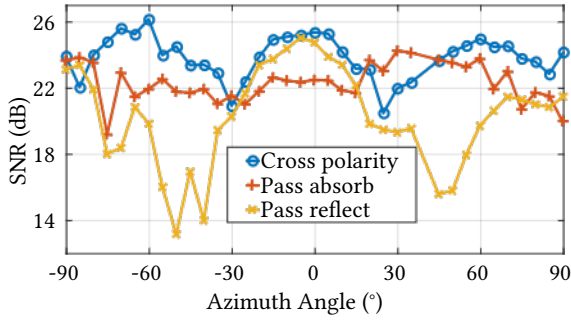
Figure 20: SNR vs. Azimuth Angle for different Van Atta switching configurations. The figure plots the SNR as a function of the rotation angles in azimuth across three different switching mechanisms: cross-polarity (blue), pass/reflect (red), and pass/absorb (yellow).

Figure 21: Impact of Impedance Mismatch. Simulation of the transmitted (blue) & reflected (orange) beams of a 2-element Van Atta unit cell.

B   SWITCHING MECHANISMS

Recall from our discussion in section §3.1, the cross-polarity switching allows us to achieve the highest SNR at the receiver as opposed to other switching mechanisms. Thus, we would like to experimentally evaluate and compare the performance of cross-polarity switching against other plausible switching techniques and assess their impact on the Van Atta retrodirectivity. This experiment was performed in the Atlantic Ocean at a depth of 3 meters in a 30-meter-deep near-shore environment. The distance between the reader and the Van Atta array was fixed to three meters. We used a unit-cell (2-element) Van Atta array in this experiment and evaluated the performance of three different switching techniques - pass/absorb (Fig.4), pass/reflect (Fig.5), and cross-polarity (Fig.6)- across different angles. The Van Atta array was rotated from -90° to 90° in steps of 5° for each of the three techniques, and at each step, we computed the SNR of the backscattered signal. We transmitted 1.8 W of power and the datarate was set to 500 bps.

Fig.20 plots the SNR of the switching methods – cross-polarity (blue), pass/absorb (red), and pass/reflect (yellow) – as a function of angle. Since the Van Atta structure is symmetrical around 180°, we only plot the results between -90° and 90°. We make the following observations:

- The cross polarity switching (blue) displays a relatively consistent SNR around 25 dB across rotations in the azimuth plane. The observed SNR fluctuations (of around 4 dB between 22 and 24 dB across angles) are due to minor impedance mismatches between the two elements of the unit cell.
- The pass/absorb (red) also maintains a stable SNR of around 22 dB vs angle. In comparison to cross-polarity, this technique experiences an average of 3 dB drop. This is expected because the cross-polarity enables retrodirectivity in both switching states, whereas the pass/absorb offers it in only one state while the other state absorbs the signal (as per §3.1).
- Finally, the pass/reflect (yellow) has a peak around 25 dB at 0° but drops to as low as 13 dB around ±45° then rises again to around 22 dB around ±90°. This large drop in SNR (more than 12dB between peak and valley) is expected and is a result of the two reflected states being indistinguishable by the receiver at certain angles.
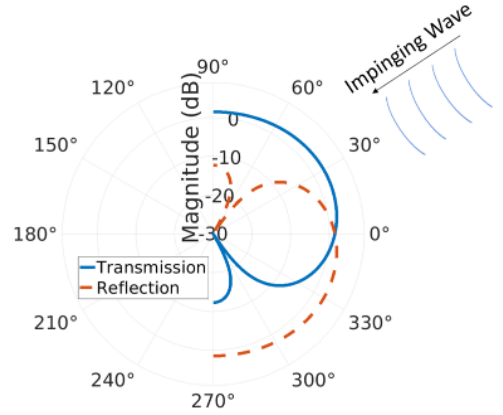
This experiment demonstrates the reliable and strong retrodirective performance offered by the cross-polarity switching mechanism, and justifies our choice for the VAB implementation.

C   IMPACT OF IMPEDANCE MISMATCH

We analyze the impact of impedance mismatch on retrodirectivity in VAB. Without impedance matching, rather than power being entirely transferred from one node to another, power received by one node will be split into two distinct waves: one that is *transmitted* to the other node, and one that is *reflected* back to the original node.[16] This happens simultaneously to both waves received on both nodes. The resulting beam pattern of the Van Atta array is then composed of two patterns: one generated by the power *transfer* between the elements–this is the useful retrodirective beam–and one generated by the power *reflection* between them. Without matching, impedance mismatches create phase errors specifically in the power reflection pattern, causing the reflection pattern to actually rotate in the *opposite* direction of the desired retrodirective pattern.

To illustrate this, consider the simplified example shown in Fig. 21, whereby an impinging wave arrives from 30°. Here, the Van Atta pair (not shown) is oriented vertically and centered at the origin of the figure. When the impinging wave arrives from 30°, each node transmits half of the power it received to the other node, but the other half is reflected off of the opposing node. The transmission portion gets retrodirected in the 30° direction as shown in blue. But there is another pattern, the reflection pattern in orange, emitting power at -30°. These two patterns sum together in the amplitude domain to create the total beam. When the two are summed, the array exhibits almost no directional selectivity and loses its retrodirective behavior. This highlights the importance of proper matching for maximum power transmission between the nodes.

D   IMPACT OF NUMBER OF ELEMENTS (N)

We performed an experiment to quantify and understand the impact of the number of array elements on the communication performance of VAB. In this experiment, we fixed the distance between

[16]For a detailed analysis of power waves in a discrete network without transmission lines, we refer the reader to [58]
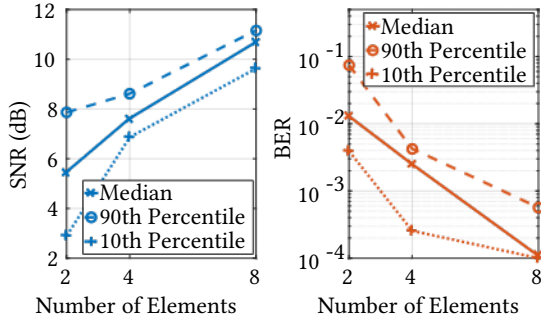
Figure 22: SNR and BER vs Number of elements. These plots show the SNR and BER performance of VAB as a function of the increasing number of elements in the array.

Figure 23: SNR vs Elevation angle. This plot shows the SNR performance of a 4x1 (blue) and a 4x2 VAB staggered arrays (red) in the elevation plane.

the Van Atta array and the reader to be 20 meters and compared the performance of a 2x1, a 4x1, and a 4x2 staggered Van Atta array at 0°, with 2, 4, and 8 elements in total respectively. For each configuration, we performed 8 trials at 500 bps.

Fig. 22 plots the median, 90th percentile, and 10th percentile of the SNR (left) and BER (right) as a function of increasing number of elements in the array. We note the following:

- As the number of elements increases from 2 to 8, the median SNR increases from 5.5 dB to 10.7 dB. Similarly, the 10th and 90th percentiles increase from 3 dB and 8 dB, respectively, to 9.5 dB and 11.2 dB, respectively. The increasing trend in SNR is expected because as the number of the elements in the array increase, the gain increases and thus the SNR is improved. This demonstrates that a larger size Van Atta is able to achieve the gain and SNR improvement at the receiver.

- Similarly, the median BER drops from 10^{-2} with 2 elements to 10^{-4} with 8 elements. A similar trend is observed with the 10th and 90th percentile decreasing from $3{\times}10^{-2}$ and $9{\times}10^{-2}$, respectively, to 10^{-4} and $4{\times}10^{-4}$, respectively. This observed BER improvement is expected as the number of elements increase due to the SNR improvement.

This experiment demonstrates the ability of a larger Van Atta to improve the SNR and BER of the system.

E 3D RETRODIRECTIVITY

We performed an experiment to evaluate the 3D retrodirectivity of our VAB design. Having demonstrated the retrodirectivity in the horizontal plane (azimuthal) with the 1D structure (in Fig. 9 and Fig. 12), we still needed to evaluate the ability to retrodirect in the elevation plane using the 2D array. We performed an experiment where we placed the 4x2 staggered Van Atta array at a 30 m distance from the reader. We rotated the array in the elevation plane from -90° to 90° in steps of 5° and compared the SNR across elevation angle to that of the 4x1 staggered Van Atta array. In this experiment, the bit rate is set to 500 bps, and the transmitted power to 1.8 W. We repeat 3 trials at each angle for each architecture, thus performing 222 experimental trials in total.

Fig. 23 plots the median SNR vs. elevation angle for both the 4x2 staggered Van Atta array (red) and the 4x1 staggered Van Atta array (blue). We make the following remarks:

- The 4x2 VAB displays a peak SNR of around 13 dB between ±15°
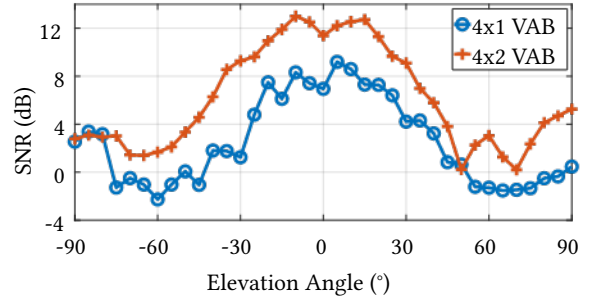
and 15° before starting to drop with the increase in elevation angle, reaching a level of 2 dB at ±75°. This drop in SNR is expected since the cylindrical node element used in this work is not omnidirectional in elevation, leading to a more limited angular coverage in that dimension (vs azimuthal). This is due to the radiation pattern of the transducer itself (not the array) and, if need be, can be addressed by leveraging spherical instead of cylindrical transducers.

- The 4x1 VAB follows the same trend with a similar coverage where the SNR drops from a peak of 9 dB (between ±15°) to approximately -3 dB (around ±75°).

- The 4x2 VAB achieves around 4-6 dB improvement over the 4x1 array. This boost in SNR is anticipated because the number of elements in the array double.

- Most importantly, what is worth noting here is that the 4-6 dB improvement in SNR is relatively consistent across angles. The consistency across angles is what shows that the retrodirective gain is indeed maintained across elevation (even though the trend itself decays around ±75° due to the transducer properties).

This result shows that our 2D architecture allows achieving the retrodirective gain in elevation, thus allows us to achieve 3D retrodirectivity taking into account that we have already demonstrated azimuthal retrodirectivity.

F FABRICATED HARDWARE

This appendix provides additional details about our fabricated hardware shown in fig.24.

Underwater Transducer. Fig. 24a shows one of our fabricated transducers, which is the core radiating element that our Van Atta arrays are composed of. To fabricate each transducer, we first solder two wires to the inner and outer surfaces of the piezoelectric cylinder, corresponding to the positive and negative terminals, respectively. We then attach these wires to a panel-mount sealed Micro-Con-X connector [59] and fix this connector to a cutout in a 3D-printed top cap. Then, we place the cylinder between the top cap and another 3D-printed bottom cap and place two circular rubber gaskets at the interfaces of the cylinder and the top and bottom caps. Once the caps, cylinder, and gaskets are in place, we tighten the entire structure down with a single M4 screw and nut that passes through the end caps and the cylinder center. Next, this assembly is placed into a 3D-printed mold slightly larger than the diameter of the piezoelectric cylinder, and fill the mold with an epoxy mixture

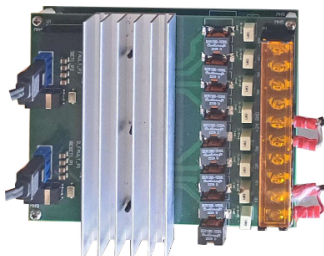(a) Transducer.　　　　(b) PCB for Matching and Switching.　　　　(c) Autorotator.
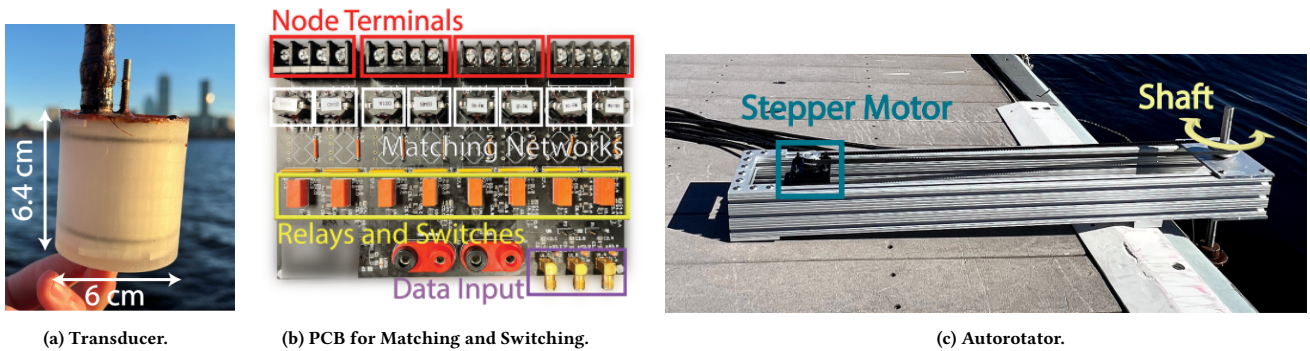
Figure 24: Fabricated Hardware. (a) A in-house fabricated epoxy transducer. (b) The custom-build switching PCB. (c) Shows the autorotator designed to rotate the submerged backscatter structure underwater.
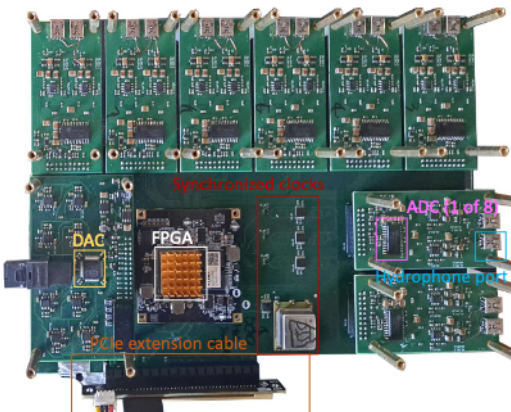
Figure 25: Custom-built reader board.

Figure 26: Custom-built power amplifier board.

[60] to achieve waterproofing and electrical insulation. We then place the mold in a pressure chamber for nearly 10 hours at 60 psi such that the epoxy hardens with no bubbles or imperfections. After removing it from the pressure chamber, we manually remove the mold and apply a layer of Scotchkote electrical coating [61] around the Micro-Con-X connector to prevent water leakage. We use this fabrication procedure to fabricate multiple nodes for the Van Atta array.

Switching PCB. Fig. 24b shows the fabricated PCB containing the switching circuitry required to perform both Van Atta cross-polarity switching and standard array switching. The PCB can support up to 8 nodes in total and incorporates the transformer-based matching described in section §3.1. We note that the core part of our electronic implementation (the TS5A2316 swtiches) is net-zero power.

Backscatter is termed a net-zero power (or passive) communication technology since it does not require generating acoustic signals or amplifying them at the backscatter device. That said, our proof-of-concept implementation includes additional components in order to compare to alternate designs under the exact same conditions. For example, the relays in Fig. 24b are exclusively used to change the path of the acoustic signal according to the desired Van Atta or array mode of operation. Similarly, while the USRP is used for prototyping, it can be easily replaced with a microcontroller for our purposes as in past underwater backscatter designs. Also, we designed the switching board to be able to measure the power consumption of only the components that contribute to backscatter switching, which in our case consumes about 6 μW when switching a 1 kHz square wave as the data input.

Autorotator. Fig. 24c shows the constructed mechanism (the autorotator) to rotate any array or single node in the water. This device contains a stepper motor with ethernet control and a belt drive to automatically rotate the structure in the water with roughly 1° of angular precision.

Reader. Fig. 25 shows the fabricated reader assembly which consists of 8 ADC module, 1 DAC module, FPGA module, and the base board with synchronized clocking. This board supports interfacing with 8 inputs from hydrophone and 8 outputs to power amplifier with the host computer with a PCIe interface. Fig. 26 shows the custom-built power amplifier module that inputs from the DAC and drives the projector with appropriate impedance matching.

G ADDITIONAL BASELINE RESULTS

Below, we report additional baseline results.

Fig. 27 shows the median BER vs. range for the single node at 500 bps, 1 kbps, and 2 kbps using the multichannel decoder. Beyond 60 m, the single node exhibited almost no backscatter signal and extremely low SNR, thus all BER results beyond 60 m were 0.5 and not shown in the figure.

Fig. 28 shows the median BER vs. range for the single node at 1.8 W and 0.11 W of transmit power using the multichannel decoder. Again, beyond 60 m the single node BER remained at 0.5.

Comparing these results to those reported in §5.3 and §5.4 reinforces the benefits of VAB over the enhanced baseline.
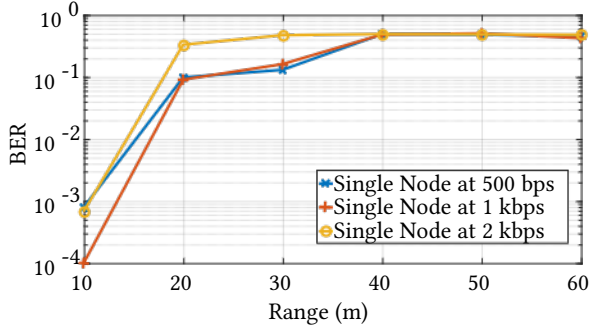
Figure 27: BER vs. Range for the enhanced baseline at different throughputs. The figure plots the BER vs range at 500 bps (blue), 1 kbps (red), and 2 kbps (yellow). The BER for all datasets beyond 60 m remained 0.5.
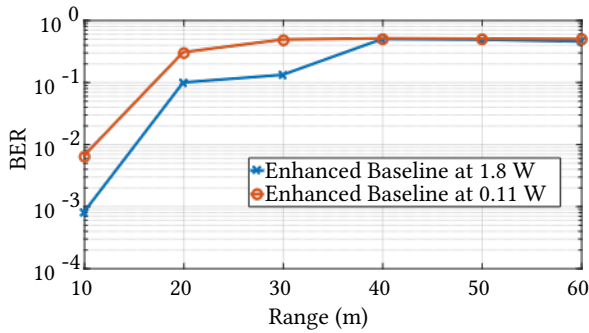
Figure 28: BER vs. Range for the enhanced baseline at different transmit power. The figure plots the BER vs range at 1.8 W (blue) and 0.11 W (red). The BER for all datasets beyond 60 m remained 0.5.

H FM0 PREPROCESSING FOR DFE

Here we elaborate mathematically how the receiving pipeline pre-process the FM0 data into BPSK samples, which is ready for the equalizer to work on. We first establish the equivalence between FM0 coding and minimum shift keying modulation, which allows us to perform subcarrier downconversion and filter the carrier leakage, and then we explain the Laurent decomposition that we use to expand the angular-modulated MSK data into the linearly-modulated partial response OQPSK and BPSK data.

H.1 MSK representation of FM0 single-side-band data

Let T be the symbol interval, $g_i \in \{0, 1\}$ the i-th encoded bits seen by MSK encoder, and $\varphi_i : \sum_{k=1}^{i-1} g_k \mod 2$. Then, the transmit FM0 encoded baseband waveform, $a(t)$, encoding the i-th bit ($iT \leq t \leq (i+1)T$) can be written and approximated as follows:

$$a(t) \quad \mathrm{sgn}\sin\left(\pi\varphi_i + \frac{\pi(2 \quad g_i)(t \quad iT)}{T}\right)$$

$$\approx \sin\left(\pi\varphi_i + \frac{\pi(2 \quad g_i)(t \quad iT)}{T}\right)$$

$$\Re\left\{\exp\left(j\left(\frac{3\pi t}{2T} \quad \frac{\pi}{2}\right)\right) \cdot \exp\left(j\pi\left(\varphi_i + \frac{i}{2} + \frac{(1 \quad 2g_i)(t \quad iT)}{2T}\right)\right)\right\}$$

$$: \Re\left\{S(t)M(t, g_i, \varphi_i)\right\}$$

We first ignore the high-frequency harmonics ($\mathrm{sgn}\sin(\cdot) \approx \sin(\cdot)$), and then factor out a constant subcarrier $S(t) \quad \exp\left(j\left(\frac{3\pi t}{2T} \quad \frac{\pi}{2}\right)\right)$,

whose frequency is $f_S \quad 0.75/T$ Hz. What remains $M(t, g_i, \varphi_i)$ $\exp\left(j\pi\left(\varphi_i + \frac{i}{2} + \frac{(1 \quad 2g_i)(t \quad iT)}{2T}\right)\right)$ becomes the canonical expression of minimum-shift keying (MSK) modulation, in which the phase term

$$i/2 + \varphi_i \quad i/2 + \sum_{k=0}^{i-1} g_k \mod 2$$

$$\frac{1}{2}\left(\sum_{k=0}^{i-1} 1 + 1 \quad (1 \quad 2g_k) \mod 4\right)$$

$$\frac{1}{2}\left(\sum_{k=0}^{i-1} 1 \quad 2g_k \mod 4\right)$$

$$\sum_{k=0}^{i-1} \frac{1 \quad 2g_k}{2} \mod 2$$

means the total rotation of $(1 \quad 2g_k)\pi/2$ of $k \quad 0..i \quad 1$ accumulates to i-th bit's waveform, establishing the phase continuity constraint in the MSK modulation. Therefore, on the receive chain in additional to the downconversion with carrier, we perform another downconversion with $S(t)$ (and $S^*(t)$) to extract the lower (and the upper, respectively) side band of FM0 as the MSK waveform. This process essentially treat each single side band (SSB) data independently, and in our evaluations since the bandwidth is sufficient, we use both of them in the multi-channel equalizer (1 physical hydrophone maps to 2 channels) to leverage frequency diversity in addition to spatial diversity.

After extracting the MSK waveform out of the FM0 data, we perform a low pass filtering with the pass band up to $0.6375/T$ and stop band beyond $0.685/T$, and this low-pass-filtered data is further resampled at $1/2T$ (2 samples per bit) without aliasing. equivalent to a band-pass filter before the $f_S \quad 0.75/T$ subcarrier downconversion, with passband of $[0.1125/T, 1.3875/T]$ and stopband of $[0, 0.075/T] \cup [1.425/T, F_{ADC}/2]$, where $F_{ADC} \quad 192\text{kHz}$ is the sampling frequency of hardware. Note that the stopband now erases the DC and low frequency components from the signal, which solves the carrier leakage problem of co-located transmitter and receiver, even if the leakage through a dynamic reflecting water surface and is time varying, as long as the wave is not likely faster than $0.075/T$.

H.2 Linear decomposition and precoding of MSK

Having arrived at the intermediate representation of MSK modulation, we focus on the Laurent decomposition, which maps the MSK waveform into a partial-response OQPSK/BPSK waveform and allows us to perform general coherent equalization on it. [17] We algebraically manipulate the MSK waveform $M(t, g, \phi)$ as follows, which is a special case of Laurent decomposition[62] that applies

---

[17]MSK/FM0 is more commonly been decoded by the Viterbi decoder, and it is theoretically possible to write an Viterbi MLSE for MSK. However, given the task of equalization on a very long channel, the exponential state space of Viterbi could be problematic.

to all continuous-phase modulation:

$$M(t, g_i, \varphi_i) = \exp\left(j\pi\varphi_i\right) \exp(j\pi i/2) \exp\left(\frac{j\pi(1 - 2g_i)(t - iT)}{2T}\right)$$

$$= (-1)^{-i} j^i \left(j \sin\left(\pi\left(\frac{(1 - 2g_i)(t - iT)}{2T}\right)\right) + \cos\left(\pi\left(\frac{(1 - 2g_i)(t - iT)}{2T}\right)\right)\right)$$

$$= (-1)^{-i} j^i \left(j(1 - 2g_i) \sin\left(\frac{\pi(t - iT)}{2T}\right) + \cos\left(\frac{\pi(t - iT)}{2T}\right)\right)$$

$$= (-1)^{i+1} j^{i+1} \sin\left(\frac{\pi(t - iT)}{2T}\right) + (-1)^{-i} j^i \cos\left(\frac{\pi(t - iT)}{2T}\right)$$

Here we expand the last complex exponential in Eular formula, leverage that $(1 - 2g_i) \in \{-1, 1\}$ and that $\sin()$ is an odd function and that $\cos()$ is an even function, and finally use $1 - 2g_i = (-1)^{g_i}$ and $\varphi_{i+1} = \varphi_i + g_i \mod 2$. Now the MSK is been represented as a function of the cumulative phase φ_i, we are ready to convert the MSK waveform into a partial response BPSK waveform. Let's define the partial response pulse shape function, $p(t)$, as

$$p(t) = \begin{cases} \exp\left(-\frac{j\pi t}{2T}\right) \cos\left(\frac{\pi t}{2T}\right), & |t| \leq T \\ 0, & \text{otherwise} \end{cases}$$

Then, to eliminate the j^i term [18], we modulate the MSK waveform for third time with $\exp(-\frac{2j\pi t}{2T})$:

$$M(t, g_i, \varphi_i) \exp(-\frac{2j\pi t}{2T})$$

$$= (-1)^{\varphi_{i+1}} j \exp\left(-\frac{j\pi(t - iT)}{2T}\right) \sin\left(\frac{\pi(t - iT)}{2T}\right)$$

$$+ (-1)^{\varphi_i} \exp\left(-\frac{j\pi(t - iT)}{2T}\right) \cos\left(\frac{\pi(t - iT)}{2T}\right)$$

$$= (-1)^{\varphi_{i+1}} \exp\left(-\frac{j\pi(t - (i+1)T)}{2T}\right) \cos\left(\frac{\pi(t - (i+1)T)}{2T}\right)$$

$$+ (-1)^{\varphi_i} \exp\left(-\frac{j\pi(t - iT)}{2T}\right) \cos\left(\frac{\pi(t - iT)}{2T}\right)$$

$$:= \sum_{k=-\infty}^{\infty} (-1)^{\varphi_{i+k}} p(t - (i+k)T)$$

This ends up with a partial-response BPSK on φ_i by definition. Therefore in our receiver, we perform the same mixing of $f_3 - 1/2T$, to reduce the receive signal in this partial-response format, and it becomes the task of the equalizer to learn and deconvolve the composite response $h'(t) = h(t) * p(t)$ from the receive signal, where $h(t)$ is the CIR in the water channel.

Note that the equalizer's output of φ_i is the just cumulative XOR-sum of the FM0 encoded bits g_i, and when the φ_i is recovered by the equalizer, we can recover the $g_i = \varphi_{i+1} - \varphi_i \mod 2$. In this approach, each wrong φ_i will flip g_i and g_{i-1}, doubling the BER which is undesirable. A better alternative is to swap the role of φ and g, let the information to be φ and let the backscatter side to compute $g_i = \varphi_{i+1} - \varphi_i \mod 2$ before feeding the FM0 encoder. This approach is known as differential precoding [62, 63].

---

[18]Otherwise, we can treat the $\varphi_i j^i$ as a whole and decode in OQPSK format.